Mon. Not. R. Astron. Soc. **000, 000–000**, (1995) Printed February 14, 2008 (MN plain TEX macros v1.6)

The Capture and Escape of Stars

J.L. Collett,[1] S.N. Dutta,[1,2] and N.W. Evans[1]
[1] *Theoretical Physics, Department of Physics, 1 Keble Road, Oxford, OX1 3NP*
[2] *Department of Physics and Astronomy, Ohio University, Athens, OH 45701-2979, USA*

ABSTRACT

The shape of galaxies depends on their orbital populations. These populations change through capture into and escape from resonance. Capture problems fall into distinct cases depending upon the shape of the potential well. To visualise the effective potential well for orbital capture, a diagrammatic approach to the resonant perturbation theory of Born is presented. These diagrams we call equiaction sections. To illustrate their use, we present examples drawn from both galactic and Solar System dynamics. The probability of capture for generic shapes of the potential well is calculated.

A number of predictions are made. First, there are barred galaxies that possess two outer rings of gas and stars (type $R_1'R_2'$). We show how to relate changes in the pattern speed and amplitude of the bar to the strength of the two rings. Secondly, under certain conditions, small disturbances can lead to dramatic changes in orbital shape. This can be exploited as a mechanism to pump counter-rotating stars and gas into the nuclei of disk galaxies. Tidal resonant forcing of highly inclined orbits around a central mass causes a substantial increase in the likelihood of collision. Thirdly, the angular momentum of a potential well is changed by the passage of stars across or capture into the well. This can lead to the creation of holes, notches and high velocity tails in the stellar distribution function, whose form we explicitly calculate.

Key words: celestial mechanics, stellar dynamics – galaxies: kinematics and dynamics – galaxies: structure – Solar system: general – planets and satellites: individual: Pluto

1 1 INTRODUCTION

Stars within galaxies belong to orbital families. The size and shape of a galaxy determines the relative populations of these families. As a galaxy evolves, capture and escape of stars between these families takes place. So, capture and escape are generic processes that will have occurred many times in the history of galaxies.

Each orbital family has a parent periodic orbit – that is, an orbit that describes a closed figure. For example, in a spherical galaxy, all stars belong to the family of tube orbits whose members librate around the closed circular orbits. An oval distortion in the centre of this galaxy is supported by the family of box orbits, whose parent periodic orbits are the radial orbits. As the distortion grows, stars are transferred from the loop to the box family. This capture process is important in the formation, maintenance and secular evolution of non-axisymmetric structures, such as bars, rings and spiral arms (e.g., Lynden-Bell 1973; Kalnajs 1973; Tremaine & Weinberg 1984). Whether or not a trapped star remains trapped may depend on the presence of a central black hole or mass concentration. Close passage can scatter a star away from its original orbit and thus cause a gradual disruption of the population of orbits.

Let us turn to some specific problems. First, some barred galaxies, such as NGC 5701, possess *two* outer rings of gas and stars. Buta (1986), who labels these galaxies $R_1'R_2'$, suggests that they may be comprised of stars on periodic orbits aligned and anti-aligned with the bar. As the bar evolves, is it possible for stars to be exchanged between the rings? Second, counter-rotating gas is present in some S0 and spiral galaxies (Bertola, Buson & Zeilinger 1992). For example, the 'evil-eye' galaxy NGC 4826 has an outer HI ring, which is counter-rotating, whilst its interior gas is co-rotating (Braun, Walterbos & Kennicutt 1992). Recently, substantial counter-rotating gas has also been reported in the spiral NGC 3626 (Ciri, Bettoni & Galletta 1995). A counter-rotating component is perhaps unsurprising if the galaxy has suffered a retrograde merger or has undergone substantial secondary accretion or infall. We shall show that counter-rotating gas and stars are susceptible to large-scale orbital shape changes under resonant perturbation. This provides a mechanism for feeding gas into the centres of galactic nuclei. In a classic paper, Tremaine & Weinberg (1984) consider the origin of frictional torques in stellar systems, showing the crucial rôle played by the transfer of stars across the resonances. The shape of the effective potential well at the resonance determines the dynamics of this process. This in turn is very sensitive to orbital shape. We consider cases in which this can lead to marked changes in the stellar distribution function, including the formation of holes and notches.

The aim of our paper is to shed light on these matters. This is made easier if we have a simple, physical picture of resonant escape and capture, which we provide in Section 2.

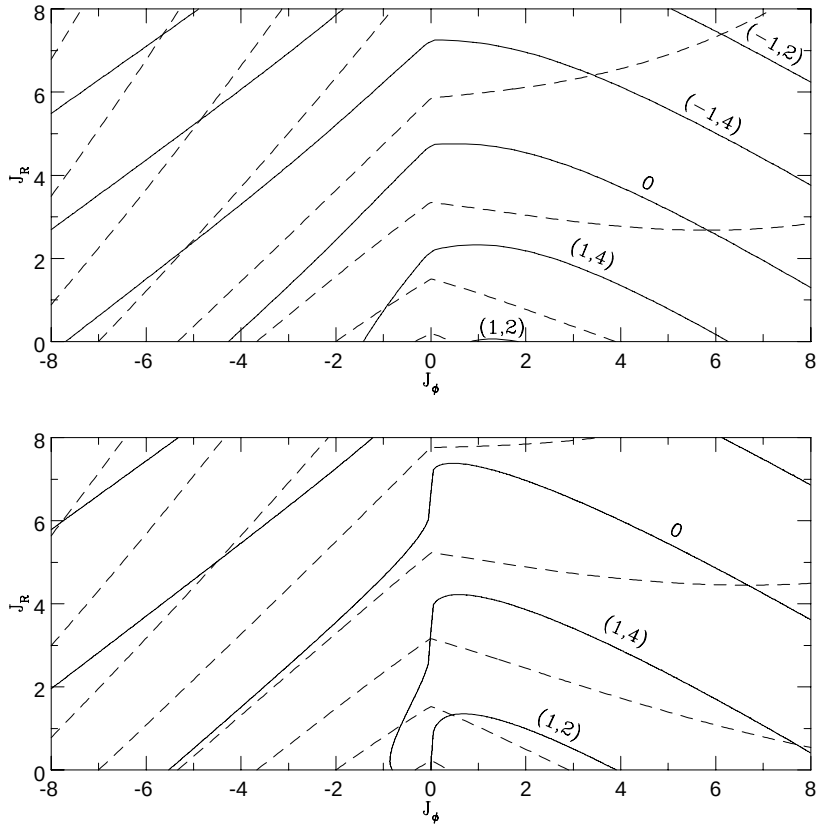

Figure 1. The solid lines represent the reticulation of the **J**-plane by (ℓ, m) resonances defined by the closure conditions [equations (2.1) and (2.6)]. The broken lines are the allowed fast action paths. They intersect a particular resonance line with the same gradient independent of the pattern speed. In the upper panel, the background potential is an axisymmetric Binney disk [equation (2.13)] and the pattern speed is taken as 0.1 (in units in which $v_0 = R_c = 1$). The lower panel shows the effects of removing the harmonic core and reducing the pattern speed. The background model is an axisymmetric Mestel disk and the pattern speed is 0.075.

2 2 THE EQUIACTION SECTION

Stellar orbits in a galactic disk nearly always form rosettes. Occasionally, the radial frequency κ and the angular frequency Ω of the star are commensurable, i.e., $\ell\kappa = m\Omega$ for some integers ℓ, m. Then, the star's orbit is periodic and it closes after m radial librations and ℓ turns around the centre. Even if the orbit is a rosette, it can be made to close by moving to a rotating frame. To an observer rotating steadily in space with angular velocity $\Omega_{\rm p}$, an orbit is closed if

$$\ell\kappa = m(\Omega - \Omega_{\rm p}). \tag{2.1}$$

An orbit meeting this condition is *resonant*. Why are the resonant orbits so important? Suppose a disturbance rotating at angular frequency $\Omega_{\rm p}$ is applied to the disk. On each traverse, the resonant stars meet the crests and troughs of the perturbation potential at the same spots in their orbits and this causes secular change in the orbital elements. The non-resonant stars feel only periodic fluctuations that average to zero. As the strength of the perturbation increases, stars near the locus of exact resonance are captured into libration around the parent periodic orbit. So, the neighbourhoods of the resonances are the regions of a galaxy where a disturbance can produce long term effects by changing populations of orbital families.

Near a resonance, the star's motion can be nicely decoupled into two disparate timescales – *fast* and *slow* oscillations (e.g., Born 1927; Lynden-Bell 1973; Tremaine & Weinberg 1984). The orbital motion is then pictured as the fast traversal of a closed figure together with the slow libration of its line of apsides. Let (R, ϕ) be polar coordinates in an axisymmetric galactic disk. Associated with the two periodic motions in radius and azimuth on our rosette orbit are actions (J_R, J_ϕ) and angles (w_R, w_ϕ) (see e.g., Born 1927; Arnold 1978). One useful property of the actions is their adiabatic invariance under slow dynamical change. The Hamiltonian H_0 of stars in the axisymmetric disk is a function of the actions alone. The frequencies κ and Ω are simply given by

$$\kappa = \frac{\partial H_0}{\partial J_R}, \qquad \Omega = \frac{\partial H_0}{\partial J_\phi}. \tag{2.2}$$

Near a resonance – where a combination of these frequencies is close to the forcing frequency (2.1) – the adiabatic invariance of (J_R, J_ϕ) breaks down. Nevertheless, there is a linear combination of actions, specific to each resonance, that is preserved, namely the circulation $\oint \mathbf{p}d\mathbf{q}$ around the closed

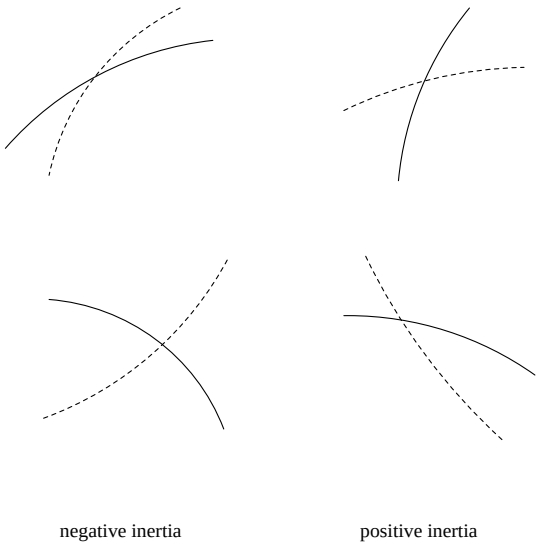

Figure 2. The sign of the inertial response of the stellar orbits may be deduced from the intersection of the resonance lines and the fast action tangent paths. The tangents to the broken lines give the local evolutionary tracks. In the left panels, $\Omega_{\rm p}$ decreases as $J_{\rm s}$ increases (negative inertia); in the right panels, $\Omega_{\rm p}$ increases as $J_{\rm s}$ increases (positive inertia). It is evident on comparison with Fig. 1 that regions of negative inertial response are preponderant. Positive inertial response, however, occurs for the negative angular momentum continuation of the $(1,4)$ resonance for the Binney disk, as well as at the inner Lindblad resonance $(1,2)$ for the Mestel disk.

figure. This is the fast action. In order to exploit this invariant, we perform at each resonance a separate canonical transformation to the corresponding slow and fast actions $(J_{\rm s}, J_{\rm f})$ and angles $(w_{\rm s}, w_{\rm f})$. This is effected by the generating function $S(J_{\rm s}, J_{\rm f}; w_R, w_\phi, t)$ (e.g., Lynden-Bell 1973; Tremaine & Weinberg 1984; Earn 1993)

$$S(\mathbf{J},\mathbf{w}) = J_{\rm s}\Big[w_\phi - \frac{\ell}{m}w_R - \int \Omega_{\rm p} dt\Big] + w_R J_{\rm f}, \tag{2.3}$$

so that

$$\begin{aligned}
&\frac{\partial S}{\partial w_\phi} = J_\phi = J_{\rm s},\\
&\frac{\partial S}{\partial J_{\rm s}} = w_{\rm s} = w_\phi - \frac{\ell}{m}w_R - \int \Omega_{\rm p} dt,\\
&\frac{\partial S}{\partial w_R} = J_R = J_{\rm f} - \frac{\ell}{m}J_\phi,\\
&\frac{\partial S}{\partial J_{\rm f}} = w_{\rm f} = w_R,\\
&\frac{\partial S}{\partial t} = -\Omega_{\rm p} J_{\rm s}.
\end{aligned} \tag{2.4}$$

Therefore, the fast and slow actions are

$$\begin{aligned}
&J_{\rm f} = J_R + \frac{\ell}{m}J_\phi,\\
&J_{\rm s} = J_\phi.
\end{aligned} \tag{2.5}$$

When the angular momentum changes sign, the resonance condition is altered (Kalnajs 1977)

$$(m-\ell)\kappa = m(\Omega + \Omega_{\rm p}), \tag{2.6}$$

where all the frequencies are taken as positive. The functional form of the fast and slow actions now becomes

$$\begin{aligned}
&J_{\rm f} = J_R - \frac{\ell}{m}|J_\phi| + |J_\phi|,\\
&J_{\rm s} = J_\phi.
\end{aligned} \tag{2.7}$$

The fast action is continuous at $J_\phi = 0$, even though its functional dependence on $\mathbf{J}$ has changed. Kalnajs (1977) gives a beautiful illustration of this point in terms of the zero angular momentum orbits which are the common limits of the (ℓ, m) and $(-\ell - m, m)$ orbits.

The reticulation of the $\mathbf{J}$-plane by the lines of exact (ℓ, m) resonance is shown in Fig. 1. The principal resonances are marked. The tangents to the broken track correspond to allowed dynamical paths because they conserve the local value of the fast action as prescribed by equation (2.5). A star trapped at a resonance oscillates along this tangent. The set of all these line elements crossing a resonance constitute a band of trapped stars, The shape and width of this band depends on the amplitude of the perturbation and the figure of the orbit. Together they determine an effective potential well in which the oscillation takes place. To construct this well, we examine the Hamiltonian of the orbits in the rotating frame.

$$\begin{aligned}
H =& H_0(\mathbf{J}) + \frac{\partial S}{\partial t} + H_{\rm p}(\mathbf{J},\mathbf{w},t)\\
=& H_0(\mathbf{J}) - \Omega_{\rm p} J_{\rm s} + H_{\rm p}(\mathbf{J},\mathbf{w},t).
\end{aligned} \tag{2.8}$$

where $H_{\rm p}$ represents the perturbation. Averaging this Hamiltonian over the fast motion leads to the following equations of motion

$$\begin{aligned}
&\frac{dJ_{\rm s}}{dt} = -\frac{\partial\langle H\rangle}{\partial w_{\rm s}} = \frac{\partial\langle\psi\rangle}{\partial w_{\rm s}},\\
&\frac{dw_{\rm s}}{dt} = \frac{\partial\langle H\rangle}{\partial J_{\rm s}} = \Omega(\mathbf{J}) - \frac{\ell}{m}\kappa(\mathbf{J}) - \Omega_{\rm p} - \frac{\partial\langle\psi\rangle}{\partial J_{\rm s}},
\end{aligned} \tag{2.9}$$

where the perturbation potential ψ can be expanded as a Fourier series over the harmonics

$$\langle\psi\rangle = \sum_{m=-\infty}^{\infty} A_m(\mathbf{J},t)\exp(imw_{\rm s}). \tag{2.10}$$

The angled brackets in equations (2.9) and (2.10) denote averages over the fast phase. If the perturbation does not depend explicitly on time, then the Hamiltonian in the rotating frame or Jacobi integral $E_{\rm J} = \langle H\rangle$ is conserved. A rough idea of the dynamics is obtained by restricting ourselves to a single harmonic component and expanding about the exact resonance to obtain the approximate equations of motion

$$\dot{J}_{\rm s} = -mA_m(\mathbf{J})\sin mw_{\rm s}, \tag{2.11a}$$

$$\dot{w}_{\rm s} = D_1(J_{\rm s} - J_{\rm r}) - \frac{\partial A_m}{\partial J_{\rm s}}\cos mw_{\rm s}. \tag{2.11b}$$

The slow angle $w_{\rm s}$ measures the inclination of the line of apsides of the figure in the trough of the well. Equation (2.11a) illustrates the angular momentum transfer when orbit and well are offset. Equation (2.11b) contains the inertial response of the orbit D_1 defined as

$$D_1 = \frac{\partial^2 H_0}{\partial J_{\rm s}^2} = \frac{\partial\Omega_{\rm p}}{\partial J_{\rm s}}. \tag{2.12}$$

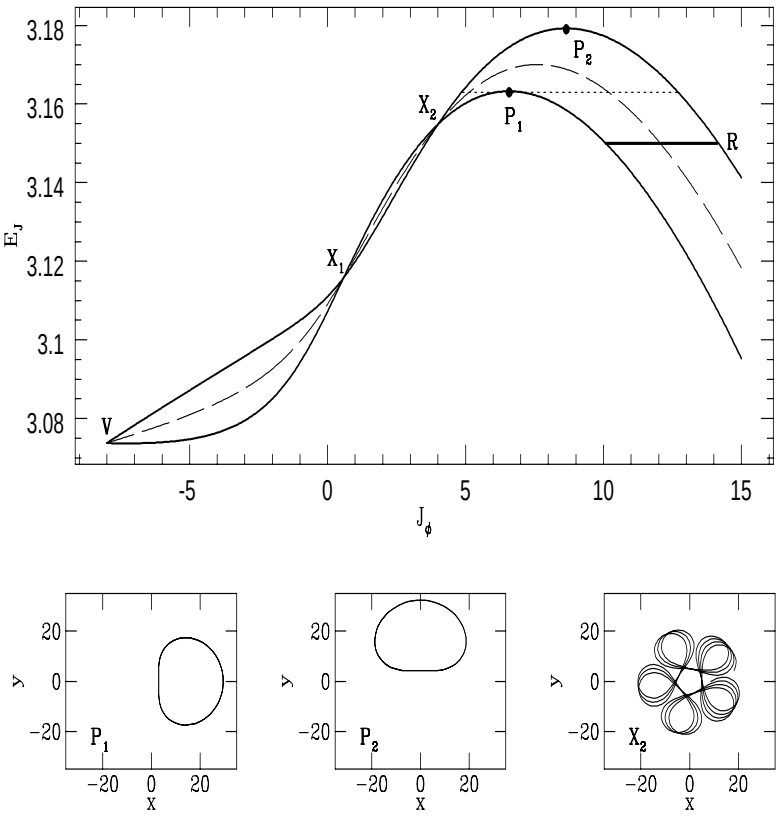

Figure 3. An equiaction section at co-rotation in the cored logarithmic model. The central seam (drawn in a broken line) represents the unperturbed Hamiltonian in the rotating frame. The upper and lower boundaries represent the full values of the Hamiltonian at the crests ($w_{\rm s} = \pi/2$) and the troughs ($w_{\rm s} = 0$). The trajectory of every star is a horizontal line on the section. Above the separatrix (dotted line), the orbits are caught into libration. Below they rotate and an example of a retrograde rotator is marked R. The periodic orbits $\rm P_1$ and $\rm P_2$ are recovered at the horizontal tangents. The planforms of the orbits are shown below the section. (The model used is (2.13) with $q = 0.85$, $\Omega_{\rm p} = 0.05$, and $J_f = 8$ in units with $v_0 = R_c = 1$). The bar axis is horizontal.

This is analogous to the reciprocal of the moment of inertia of a rigid body. Near-resonant orbits have the curious property that their angular inertia depends on the forcing frequency. The inertial response of an orbit is positive when its angular velocity is increased by an applied torque *as the fast action is held fixed.* Any orbit will have a different inertial response at different pattern frequencies because the fast action changes. Let us remark that we are following the notation of Tremaine & Weinberg (1984) in writing D_n as the nth derivative of $\Omega_{\rm p}$ with respect to $J_{\rm s}$. Earn & Lynden-Bell (1996; see also Earn 1993) refer to D_1 as the cooperation parameter in their studies of disc models which have regions of both positive and negative inertial response.

Fig. 2 shows how the inertial response of orbits can be deduced from the intersections of the fast action tangents with the resonance lines. When the resonance line and fast action tangent are nearly parallel, the orbit possesses very large inertia and is able to move some distance along the tangent without moving far from exact resonance. The gradient term in (2.11b) will be of particular importance when we investigate the capture and release of resonant orbits in section 3.

We shall examine the trajectories of equations (2.9) in a slice through phase space at constant fast action. These surfaces we call equiaction sections (Evans & Collett 1994; Collett 1995). The effective potential well takes different forms in different sections. We now consider specific examples of such sections at the three principal resonances – the corotation $(0, 2)$ and the inner and outer Lindblad resonances $(\pm 1, 2)$. Low order resonances are the most important because the resonant orbits display the most marked deviations from axisymmetry and therefore couple most strongly to simple non-axisymmetric patterns.

The equiaction sections can be compared to Poincaré surfaces of section (see e.g., Gutzwiller 1990). These have been used extensively, for instance, by Contopoulos and collaborators to map the orbital structure of bar-like potentials (e.g., Contopoulos & Papayannopoulos 1980). Our interest here is in time-dependent problems and the equiaction sections have the advantage that the changes in orbital families are more clearly depicted. Donner (1979) drew diagrams reflecting the pendulum-like solutions of the equations (2.9) very close to the exact resonance. These are related to equiaction sections, but the trajectories of stars were

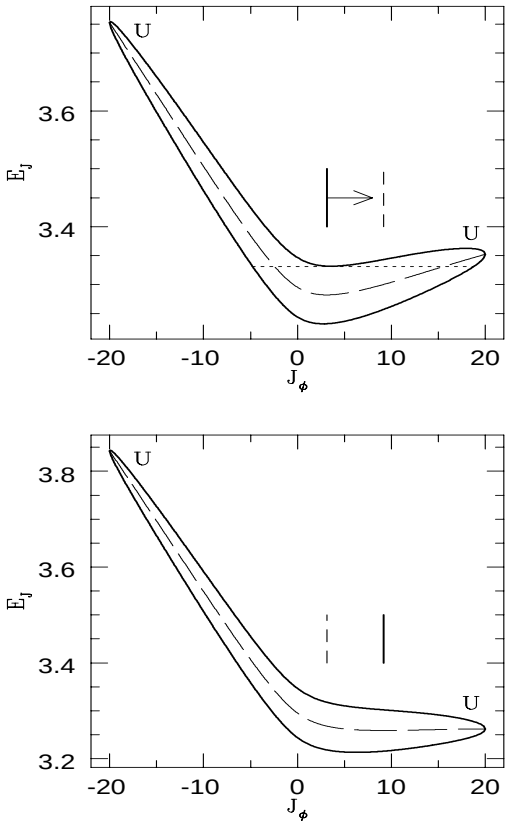

Figure 4. When the pattern speed changes, the position of exact resonance moves along the section. The first panel shows the equiaction section for the Binney disc with $q = 0.9, \Omega_{\rm p} = 0.01$ and $J_{\rm f} = 10$. The second panel is the section taken at the same value of the fast action, but with the higher pattern speed $\Omega_{\rm p} = 0.0145$. In this example, the section becomes flatter as the pattern speed is increased. This makes the box orbits fatter.

parabolae rather than the straight lines here.

2.1 2.2 Co-rotation ($\ell = 0$) resonance

At co-rotation, the resonant orbits are, for near-circular orbits, Lindblad epicycles. Their small size means that they can feel a significant orbit-averaged potential (because they sample the perturbing potential in a small patch). This diminishes as the orbit becomes larger, except when the perturbations has the same symmetry as the orbit. The conserved fast action is the radial action [see equation (2.5)] – in Fig. 1, the fast action tangents that intersect the ($\ell = 0$) resonance line are horizontal. When we draw an equiaction section, we extend this tangent and then make our cut. When the cut reaches $J_\phi = 0$, it changes direction in accord with the new fast action (2.7).

In our dynamical model, the underlying Hamiltonian H_0 is that of the axisymmetric cored Mestel (1963) disk. The rotating disturbance, H_p, is a pure $m = 2$ component, so that

$$H = H_0 + H_p = \tfrac{1}{2}p_R^2 + \tfrac{1}{2}\frac{p_\phi^2}{R^2} + \tfrac{1}{2}\log(\tilde{R}_c^2 + R^2) + \epsilon\frac{R^2}{\tilde{R}_c^2 + R^2}\cos 2(\phi - \int \Omega_{\rm p} dt). \quad (2.13)$$

When $\epsilon = (1-q^2)/(1+q^2)$ and $R_c^2 = \frac{1}{2}\tilde{R}_c^2(1+q^{-2})$, then the entire Hamiltonian replicates the weakly non-axisymmetric rotating Binney disk (see Binney 1982; Binney & Tremaine 1987, p. 126)

$$H = \tfrac{1}{2}p_R^2 + \tfrac{1}{2}\frac{p_\phi^2}{R^2} - \Omega_{\rm p}p_\phi + \tfrac{1}{2}\log(R_c^2 + x^2 + y^2q^{-2}). \quad (2.14)$$

The density corresponding to the potential (2.13) is positive for $0 \le q \le 1$. Using this Hamiltonian, a typical equiaction section is drawn at co-rotation in Fig. 3. The central seam is the unperturbed Hamiltonian in the rotating frame, $H_0(\mathbf{J}) - \Omega_{\rm p}J_{\rm s}$. The curvature of the central seam has a simple physical interpretation. When the curvature is downward, as it is rightward of point X_1 in Fig. 3, then the inertial response (2.12) is negative. The envelope of the equiaction section is drawn by finding the orbit-averaged perturbation potential, $\langle\psi\rangle$. This provides the effective potential within an equiaction section. (A simple mechanical model of this is provided by the jointed arm of Appendix A). For each orbit, $\langle\psi\rangle$ is computed in the particular rotating frame in which the orbit closes. Since orbits conserve the Jacobi integral in the frame of the perturbation, they are horizontal lines on an equiaction section, internal to and bounded by the envelope. The shape of the envelope governs the range of the angular momentum exchange of each orbit with the perturbation. The periodic orbits P_1 and P_2 are recovered at the horizontal tangents and experience no angular momentum exchange. These orbits bifurcate, or split, from the position of exact resonance, which corresponds to the maximum of the central seam. The splitting of the orbits is obtained from (2.9) as

$$\Delta J_{\rm s} = 2\frac{\partial\langle\psi\rangle}{\partial\Omega_{\rm p}}. \quad (2.15)$$

P_2, though at a maximum of the effective potential, is stable in the sense that orbits close by librate about it. P_1 is unstable for it will, if disturbed, either rotate if it loses energy or perform a large amplitude libration about P_1 if it gains energy. The dotted horizontal line is a separatrix, above which the stars are trapped. Below the separatrix, the orbits are retrograde rotators to the right (an example of which is the horizontal line labelled R) and prograde rotators to the left.

The capture and scattering between orbital families depends critically on the shape of the envelope close to the resonance. Particularly interesting dynamics can occur when the resonance lies close to points at which the envelope crosses or meets the seam (when the gradient term in (2.11) becomes important). There are three cases of special interest:
(1) U points, where the envelope terminates on the seam at a point corresponding to the circular orbit $J_{\rm circ}$ and the amplitude A_m is proportional to $|J - J_{\rm circ}|^{1/2}$,
(2) V points, where the envelope terminates on the circular orbit, but the amplitude A_m is now proportional to $|J - J_{\rm circ}|$,
(3) X points, where the envelope crosses the seam and $A_m \propto |J - J_{\rm circ}|$.

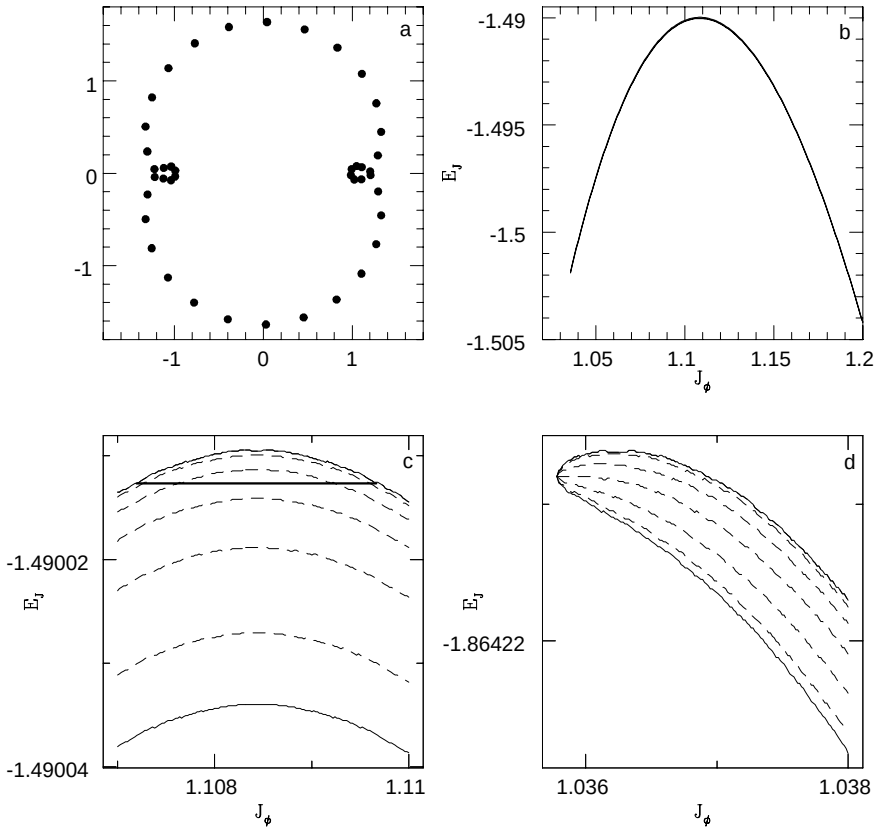

Figure 5. (a) The closed orbit of Pluto in the frame co-rotating with the mean motion of Neptune is shown. The time interval between the plotted points is $\sim 4,500$ days. The axis of the line of apsides librates with an amplitude of $\sim 38°$. (b) The present-day equiaction section of Pluto. Pluto has worked its way rightwards along the section as Neptune's orbit expanded. (c) A detail of the resonant part of the section. The dashed lines show the dependence of the energy on the orientation of the figure. They correspond to inclination angles of $15°, 30°, 45°, 60°$ and $75°$ of the line of apsides. The influence of many harmonics in the potential is evident in the dispersal of these contours. The present day orbit of Pluto is shown as a bold horizontal line. (d) A detail of the tip of the section when the radius of Neptune was $\sim 82\%$ of its present value and Pluto was trapped from a near-circular orbit. At the initial capture, the $m = 2$ component in the perturbing potential was dominant, as indicated by the symmetric placing of the dashed lines. [All the equiaction sections are drawn with $J_{\rm f} = -0.518$ in units with $G = {\rm M}_\odot = r_{\rm N} = 1$].

In Fig. 3, we see three points where the orbit-averaged potential vanishes. The leftmost point of the equiaction section is a V-point and corresponds to a circular orbit. Further along the equiaction section, the orbit-averaged potential changes sign twice. These crossing points are X-points. The occurrence and position of X-points depends on the radial form of the perturbation potential encountered by the eccentric orbits along the section. X-points are particularly common for minor resonances where the orbital shape is quickly changing. The dynamics close to an X-point, and its consequences for angular momentum transport, are explored in Section 3.1.

2.2 2.3 Inner $(1, 2)$ and Outer $(-1, 2)$ Lindblad resonance

Fig. 4 shows equiaction sections for an inner Lindblad resonance (ILR). The form of the sections here is of particular interest because, amongst the principal resonances, the inner Lindblad resonant frequencies are the most slowly varying with radius in galaxies. The curvature of the central seam may now be upward corresponding to positive inertial response. The figure presents a pair of equiaction sections showing the orbital families associated with a decelerating bar. The trough of the well is in each case represented by the lower boundary of the section, the crest of the well by the upper boundary. As the pattern speed increases, the position of exact resonance moves rightwards (as the inertial response is positive). This is indicated by the arrow. In the lower panel, the end of the section is markedly flatter, showing that the angular momentum and orbital shape varies substantially during a libration.

The envelope closes with a characteristic tip, labelled U on the figure. This is different from the V-tip found at corotation. Although it is often the case in dynamics that librators are divided from rotators by a separatrix, or oscillation of infinite period, this does not necessarily happen close to these tips. The dividing line between the rotators and librators runs through the circular orbit. The escape from trapping occurs through the circular orbit, on which the torque

vanishes. An example of this class of trapped motion is provided by the Galilean satellites, Io, Europa and Ganymede. Europa is at ILR with respect to Io and Ganymede at ILR with respect to Europa. This configuration is maintained by the small eccentricity stabilisation mechanism (e.g., Lynden-Bell & Kalnajs 1972; Peale 1976; Goldreich & Tremaine 1981; Binney & Tremaine 1987, p. 151), in which the eccentricity forced upon the near-circular orbit leads to the ensnaring torque. A mechanism such as tidal torquing – which circularises the periodic orbit by pushing it towards the end of the tip – weakens the coupling of the satellites.

An example of the class of trapped motion in which there is a separatrix is provided by Neptune and Pluto (the large eccentricity stabilisation mechanism of Peale (1976)). Pluto's eccentric orbit forms an almost closed figure in the frame of Neptune's mean motion (Cohen & Hubbard 1965; see also Fig. 5(a)). Pluto lingers in "the ears" of the orbit and the net torque then tries to align the major axis of the orbit with Neptune's position. This is an outer Lindblad resonance ($\ell = -1, m = 2$). In order to draw an equiaction section for this problem, the point mass perturbation from Neptune must be time-averaged around the closed figure of Pluto. The potential contains many more components than the single harmonics considered above. The monopole merely contributes a constant to the orbit-averaged potential, whereas the dipole vanishes if the centre of mass does not move. Neptune is effectively replaced by two masses $\frac{1}{2}M_{\rm N}$ placed at the radius of Neptune's orbit $r_{\rm N}$ and arranged fore and aft of the sun. Fig. 5 shows the full equiaction section for Pluto and two expanded details. Note that in the outer Lindblad resonant sections, the curvature of the central seam is downward, reflecting the negative inertial properties of the stars in a Keplerian potential. The upper and lower boundaries of the section now generally correspond to the trough and the crest of the potential well, reversing the roles they had at the inner Lindblad resonance. This is obvious from Fig. 5(a), as Pluto's averaged potential is most negative when the long-axis of its orbit is aligned with the trough of the well and so the "ears" are aligned with the crest.

Malhotra (1993) has suggested that Pluto was initially captured from a near-circular orbit. As Neptune was driven outwards by planetisimal expulsion, Pluto's orbit expanded but remained trapped. It moved rightwards along the section and its eccentricity increased. Its initial and present positions on the section are illustrated in the details. They are calculated by taking the present day eccentricity of Pluto as 0.25 (Allen 1973). In units in which $r_{\rm N} = G = {\rm M}_\odot = 1$, it follows that the conserved fast action of Pluto $J_{\rm f} = -0.517$. Fig. 5(b) shows the complete equiaction section of Pluto. Its thinness is in striking contrast to the earlier sections dealing with galactic resonances. This graphically illustrates one of the important differences between celestial mechanics and galactic dynamics. Non-axisymmetric disturbances in the solar system are comparatively feeble. Fig. 5(c) is an expanded detail of the resonant portion of Fig. 5(b). The bold horizontal line shows the present-day orbit of Pluto, showing the 38° amplitude of libration of the line of apsides (Cohen & Hubbard 1965). The dashed lines show the dependence of the averaged potential on the relative orientation of the figure of Pluto and Neptune. In its present position, the influence of many harmonics is clear in the asymmetrical dispersal of the contour lines. If Pluto was captured from a circular orbit, then – assuming the constancy of the fast action – this must have occurred when the radius of Neptune's orbit was 24.6 AU, or 82% of its present value. Fig. 5(d) shows the point of capture. Note that when the resonance is near the circular orbit, the perturbation is dominated by a single $m = 2$ harmonic. This process is reversible, so that were Neptune's orbit to contract, Pluto's eccentricity would be reduced. This will be true, too, of galactic stars, as a massive black hole slowly descends into the galactic centre. Stars on eccentric orbits may be caught as the resonance moves to a region of greater frequency and released at smaller eccentricities when the amplitude contracts and the curvature of the section decreases. Indeed, each star may pass through a succession of resonances during this process, so that its motion in the **J**-plane approximates to a series of small linear steps, parallel in each case to the appropriate fast action.

3 3 CAPTURE AND ESCAPE

Suppose Neptune's orbit continues to expand. Will Pluto remain trapped forever? Provided the evolution remains adiabatic, it is the shape of the section that describes the ultimate fate of Pluto. Two changes occur in the section. First, the position of exact resonance moves outwards and the curvature of the section is correspondingly decreased. Second, the restoring torque diminishes and the envelope constricts. Both effects lead to a slow increase in the amplitude of libration and eventually Pluto may escape from Neptune's grasp.

The issues of escape and capture are the subject of our attention here. The investigation of resonant capture in astronomy begins with Goldreich's (1965) explanation of the occurrence and maintenance of commensurable motions in the solar system. Subsequently, Yoder (1973, 1979) gave a diagrammatic method of calculating capture probabilities for pendulum-like systems, while Henrard (1982) devised a general treatment for any problem with one degree of freedom based upon the use of adiabatic invariants. A comprehensive summary of the classical work is contained in Henrard (1993).

Suppose a potential well of fixed amplitude has a slowly changing pattern speed. As each star along the section encounters the well, it may be captured or pass across the well and escape into counter-rotation. Our ignorance of the exact phase at which the star encounters the well's separatrix means that we must allocate probabilities to these two motions. These probabilities reflect the relative growth of the phase areas associated with the two modes of motion. This can be deduced from the shape of the separatrix, which in turn is set by the form of the section. We can distinguish three regimes which need separate treatment. These are (i) in the vicinity of an X-point or V-point, (ii) near a U-point and (iii) in a region of slow variation in the amplitude of the envelope (e.g., such as close to $\rm P_1$ in Fig. 3). Of course, capture probabilities have been calculated before in the context of celestial mechanics (e.g., Henrard & Lemaître 1983; Borderies & Goldreich 1984). Here, we shall present modified and generalised forms of these expressions, appropriate to galactic resonances.

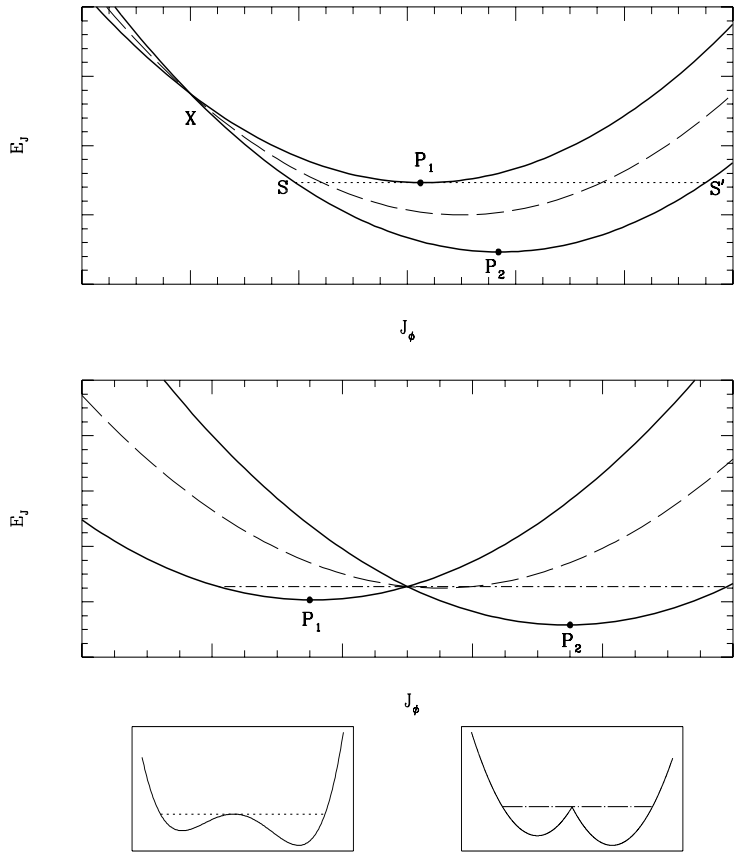

Figure 6. The upper panel shows the generic features of an equiaction section when a resonance lies close to an X-point. The periodic orbits P_1 and P_2 are equally spaced on either side of exact resonance. The separatrix SS′ divides the librating family associated with P_2 from the two sets of rotators – in this case, prograde above P_1S' and retrograde above SP_1. As the pattern speed is decreased, the position of exact resonance moves towards the X-point. A critical point is attained when P_1 reaches the X-point. Beyond this, the equiaction section takes the form shown in the lower panel with both P_1 and P_2 siring families of librating orbits. Above the dot-dashed line, the orbits are still rotators. Note that this line divides librators from rotators, but does not correspond to an orbit of infinite period. It is a pseudo-separatrix. The difference between a separatrix and a pseudo-separatrix is illustrated in the two small boxes. They show one-dimensional motion in two different double potential wells. When a cusp separates the wells, there is a pseudo-separatrix.

3.1 3.1 Capture Probabilities near X- and V-points

The Hamiltonian close to an X-Point may be written

$$H(J,w) = H_0(J,w) + A_2(J - J_{\rm X})\cos 2w. \tag{3.1}$$

Here, $J_{\rm X}$ is the critical action corresponding to the X-point and A_2 is a constant describing the amplitude of the well. Although (3.1) corresponds to the special case of the $m = 2$ harmonic, our method of derivation is general. When the position of exact resonance lies close to the X-point, the Hamiltonian may be Taylor expanded to give

$$H(J,w) = \tfrac{1}{2}D_1(J - J_{\rm r})^2 + A_2(J - J_{\rm X})\cos 2w. \tag{3.2}$$

Here, $J_{\rm r}$ is the point of exact resonance and we assume that D_1 does not vanish, although, of course, it may be either positive or negative depending on the sign of the inertial response. Now, we linearly translate the action $J \to J - J_{\rm X}$, so that the Hamiltonian has the canonical form (dropping unimportant additive constants)

$$H(J,w) = \tfrac{1}{2}D_1J^2 - D_1J(J_{\rm r} - J_{\rm X}) + A_2J\cos 2w. \tag{3.3}$$

There are three parameters in (3.3), namely D_1, A_2 and the difference $J_{\rm r} - J_{\rm X}$. As this generic problem is invariant under scaling, we introduce the dimensionless action $\tilde{J}$

$$\tilde{J} = \tfrac{1}{2}\left|D_1\frac{J}{A_2}\right|. \tag{3.4}$$

Our problem is now characterised by a single parameter $\lambda = \frac{1}{2}|D_1(J_{\rm r} - J_{\rm X})/A_2|$. (When $J_{\rm r} \approx J_{\rm X}$, this is just $\frac{1}{2}|\Delta\Omega/A_2|$, where $\Delta\Omega$ is the offset of the X-point resonant pattern speed). The scaled Hamiltonian is very simple, namely:

$$\tilde{H} = \tilde{J}^2 - 2\lambda\tilde{J} + \tilde{J}\cos 2w. \tag{3.5}$$

The periodic orbits or equilibria are the fixed points of Hamilton's equations. The stable equilibrium has coordinates $(\tilde{J} = \lambda + \frac{1}{2}, w = \frac{\pi}{2})$ and is marked P_2 in the upper panel of Fig. 6. The unstable equilibrium has coordinates $(\tilde{J} = \lambda - \frac{1}{2}, w = 0)$ and is marked P_1. When the position of exact resonance gets too close to the X-point, the unstable equilibrium disappears. As it crosses, it becomes a second stable equilibrium point P_1 marked on the lower panel of

Fig. 6. The behaviour at a V-point is similar to that at an X-point. If the X-point is stationary, it is an immutable barrier. Stars, however, can pass from one side of an X-point to another if the X-point itself is in motion, which can happen when the perturbation's radial shape changes.

To calculate capture probabilities, we must work out how the phase area of the trapping region changes along the section (this is quoted as 'Kruskal's theorem' in Cary, Escande & Tennyson 1986). So, we need to evaluate the actions associated with the two branches of the separatrix SP_1 and $\mathrm{P}_1\mathrm{S}'$ marked on the upper panel of Fig. 6. The separatrix is a level curve of the Hamiltonian (3.5). The value of the Hamiltonian marking the separatrix is (inserting the action-angle coordinates of P_1)

$$H_{\mathrm{sep}} = -\lambda^2 + \lambda - \tfrac{1}{4}. \tag{3.6}$$

The points S and S′ are the two solutions of (3.5) with $H = H_{\mathrm{sep}}$ and $w = \frac{\pi}{2}$. The actions corresponding to these points are

$$\tilde{J}_{\mathrm{S}} = \lambda + \tfrac{1}{2} - \sqrt{2\lambda}, \qquad \tilde{J}_{\mathrm{S}'} = \lambda + \tfrac{1}{2} + \sqrt{2\lambda}. \tag{3.7}$$

The equation of the separatrix is

$$\tilde{J}(w) = \lambda - \tfrac{1}{2}\cos 2w \pm [2\lambda \sin^2 w - \tfrac{1}{4}\sin^2(2w)]^{1/2}, \tag{3.8}$$

where the negative sign corresponds to the branch SP_1 (retrograde rotators when D_1 is positive as in Fig. 6, prograde rotators when D_1 is negative) and the positive sign to the branch $\mathrm{P}_1\mathrm{S}'$ (prograde rotators when D_1 is positive, retrograde rotators when D_1 is negative). It is now straightforward to evaluate the actions of the trapped orbit and the prograde and retrograde rotators near the separatrix of Fig. 6. This leads to the phase areas enclosed by these orbits:

$$\begin{aligned} S_{\mathrm{ret}} &= \lambda \operatorname{acos}\Big(\frac{1}{\sqrt{2\lambda}}\Big) - \tfrac{1}{2}(2\lambda - 1)^{1/2}, \\ S_{\mathrm{prog}} &= \pi\lambda - \lambda \operatorname{acos}\Big(\frac{1}{\sqrt{2\lambda}}\Big) + \tfrac{1}{2}(2\lambda - 1)^{1/2}, \\ S_{\mathrm{trap}} &= \pi\lambda - 2\lambda \operatorname{acos}\Big(\frac{1}{\sqrt{2\lambda}}\Big) + (2\lambda - 1)^{1/2}. \end{aligned} \tag{3.9}$$

To calculate capture probabilities, we find out how these three areas change under infinitesimal variations of the parameter λ. They are constrained by the conservation of phase area, so that here

$$\frac{dS_{\mathrm{trap}}}{d\lambda} = \frac{dS_{\mathrm{prog}}}{d\lambda} - \frac{dS_{\mathrm{ret}}}{d\lambda} = 0. \tag{3.10}$$

The general expression for the capture probability is provided by Henrard (1993) as:

$$P = \frac{\dfrac{dS_{\mathrm{trap}}}{d\lambda}}{\dfrac{dS_{\mathrm{trap}}}{d\lambda} + \dfrac{dS_{\mathrm{ret}}}{d\lambda}} = \frac{\dfrac{dS_{\mathrm{prog}}}{d\lambda} - \dfrac{dS_{\mathrm{ret}}}{d\lambda}}{\dfrac{dS_{\mathrm{prog}}}{d\lambda}}. \tag{3.11}$$

For the problem at hand, the probability of capturing a prograde rotator becomes

$$P = \frac{\pi - 2\operatorname{acos}\Big(\dfrac{1}{\sqrt{2\lambda}}\Big)}{\pi - \operatorname{acos}\Big(\dfrac{1}{\sqrt{2\lambda}}\Big)} = \frac{2}{1 + \dfrac{\pi}{2\operatorname{asin}(\frac{1}{\sqrt{2\lambda}})}}. \tag{3.12}$$

Note that $1/2 < \lambda < \infty$. Using different methods and within the context of celestial mechanics, this formula was derived for capture at a V-point by Yoder (1973). We have shown the same result is valid for capture at an X-point. The difference, however, is that the periodic orbit P_1 disappears at a V-point, but crosses and sires a librating family at an X-point.

3.2 3.2 Capture Probabilities near U-points : The Two Ring Problem

A V-point is obtained, for example, when a $(-1, 1)$ resonant orbit is subjected to a pure $m = 2$ harmonic. In a perturbation which shares the lop-sided ($m = 1$) symmetry of the orbit, the section possesses a U-point. In the first case, $\langle\psi\rangle$ depends on the square of the eccentricity e^2; in the second case, $\langle\psi\rangle \propto e$. This is evident in Fig. 5(d), where the end of the section is dominated by the $m = 2$ component. Generally, we will find a U-point for any near-circular resonant orbit in the presence of a perturbation with the same symmetry.

As the methods of derivation are the same as in the previous section and the result is well-known in celestial mechanics, we shall just quickly sketch the theory before passing on to applications. The Hamiltonian in the rotating frame near the U-point is

$$H(J, w) = H_0(J, w) + A_2|J - J_{\mathrm{circ}}|^{1/2}\cos 2w, \tag{3.13}$$

where J_{circ} is the action of the circular orbit at the very tip. On Taylor expansion about the resonant action J_{r}, this yields the Hamiltonian:

$$H(J, w) = \tfrac{1}{2}D_1(J - J_{\mathrm{r}})^2 + A_2|J - J_{\mathrm{circ}}|^{1/2}\cos 2w. \tag{3.14}$$

By defining scaled action-angle coordinates,

$$\tilde{J} = 2^{1/3}\Big|\frac{D_1}{A_2}\Big|^{2/3}|J - J_{\mathrm{circ}}|, \qquad \tilde{w} = w/2. \tag{3.15}$$

the Hamiltonian can be cast into Henrard's (1993) form

$$\tilde{H} = \tilde{J}^2 - 2\lambda\tilde{J} - 2(2\tilde{J})^{1/2}\cos\tilde{w}, \tag{3.16}$$

where

$$\lambda = 2^{1/3}\Big|\frac{D_1}{A_2}\Big|^{2/3}|J_{\mathrm{r}} - J_{\mathrm{circ}}|. \tag{3.17}$$

It is useful to introduce the canonical coordinates

$$x = (2\tilde{J})^{1/2}\cos\tilde{w}, \qquad y = (2\tilde{J})^{1/2}\sin\tilde{w}, \tag{3.18}$$

so that the scaled Hamiltonian becomes

$$\tilde{H} = \tfrac{1}{4}(x^2 + y^2)^2 - \lambda(x^2 + y^2) - 2x. \tag{3.19}$$

The equilibria satisfy

$$x^3 - 2\lambda x - 2 = 0, \qquad y = 0. \tag{3.20}$$

The three roots of the cubic correspond to two stable and one unstable equilibria. The coordinates of the unstable fixed point are:

$$x_u = -\Big(\frac{2\lambda}{3}\Big)^{1/2}(\cos\Delta + \sqrt{3}\sin\Delta), \qquad y_u = 0, \tag{3.21}$$

where Δ is defined as

$$\Delta = \tfrac{1}{3}\operatorname{acos}\Big(\frac{3}{2\lambda}\Big)^{3/2}. \tag{3.22}$$

For convenience, let us define $x_\star = -x_u$. This quantity will play an important rôle in what follows, so let us explicitly

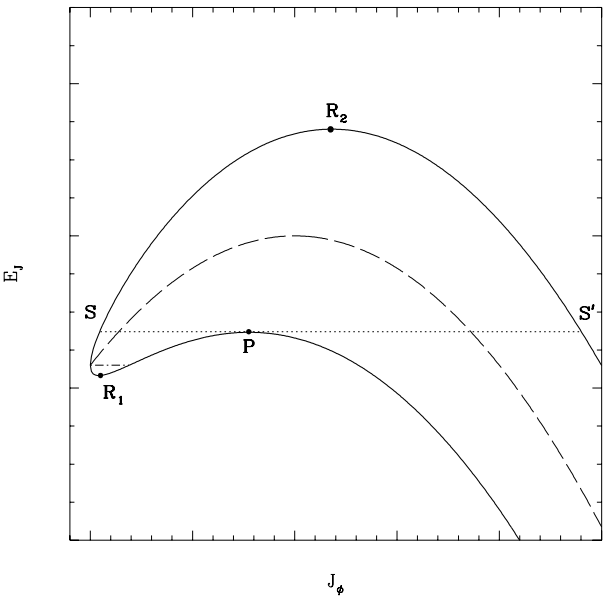

Figure 7. The anti-aligned (R_1) and aligned (R_2) periodic orbits when a resonance lies close to a U-point. These orbits build the two rings in $R_1'R_2'$ galaxies. The unstable periodic orbit P divides the separatrix (drawn as a dotted line) into two unequal branches SP and PS′. Above R_1, there is a pseudo-separatrix – shown as a dot-dashed line. Although this divides librators from rotators, it does not correspond to an orbit of infinite period.

note that it is always related to the scaled action of the unstable fixed point $\tilde{J}_{\rm u}$ by

$$\tilde{J}_{\rm u} = \tfrac{1}{2}x_\star^2. \tag{3.23}$$

If we choose $D_1 < 0$, then the separatrix looks like that of Fig. 7 with retrograde rotators below PS′ and prograde rotators below PS. Then, by evaluating the actions of these two branches of the separatrix, we find:

$$\begin{aligned} S_{\rm ret} &= \pi\lambda + 2\lambda\,\mathrm{asin}(x_\star^{-3/2}) + \frac{3(x_\star^3-1)^{1/2}}{x_\star}, \\ S_{\rm prog} &= \pi\lambda - 2\lambda\,\mathrm{asin}(x_\star^{-3/2}) - \frac{3(x_\star^3-1)^{1/2}}{x_\star}, \\ S_{\rm trap} &= 4\lambda\,\mathrm{asin}(x_\star^{-3/2}) + \frac{6(x_\star^3-1)^{1/2}}{x_\star}. \end{aligned} \tag{3.24}$$

Obviously, the area of the trapping region increases away from the tip. The probability of capturing a retrograde rotator is

$$P = \frac{2}{1+\dfrac{\pi}{2\,\mathrm{asin}(x_\star^{-3/2})}}. \tag{3.25}$$

This result was previously obtained by Yoder (1973) and Henrard & Lemaître (1983). Although the final expression is quite complicated, the important point is that the capture probability is a monotonically decreasing function of λ. As we move away from the tip, the area of the trapping region increases but its rate of swelling diminishes.

A problem which involves analysis at the U-point is that of the two outer rings. Some barred galaxies like NGC 5701 or A1340.6-2541 possess two outer rings of gas and stars (see figures 2 and 5 of Buta 1986). Can stars be transferred between the rings? As the pattern speed or the amplitude of the bar changes, which one of the two rings grows?

Fig. 7 shows an equiaction section at outer Lindblad resonance. The innermost ring is built from stars moving on periodic orbits oriented at right angles to the trough of the potential well (such as R_1 on Fig. 7). Likewise, the outermost ring corresponds to stars moving on aligned periodic orbits R_2 (see e.g., Athanassoula et al. 1982; Athanassoula & Bosma 1985). Suppose the pattern speed is diminished. As the inertial response is negative, the position of exact resonance moves outward (to higher angular momentum and therefore rightwards on the equiaction section). This is indicated by the arrow on Fig. 7. Then, the region of retrograde rotators (below PS′) shrinks in size, while the region of prograde rotators (below SP) increases. As a retrograde rotating star reaches the separatrix, it may be captured into libration or escape into the region of prograde rotation. There is no transference of trapped stars to prograde rotators, as the well is growing and the adiabatically invariant action binds stars deeper with the separatrix. In other words, all the transitions are from retrograde rotators to trapped stars or to untrapped prograde rotators. This is reversible, so that if the pattern speed is increased, then all the transitions are from trapped stars or prograde rotators to retrograde rotators. This has the interesting consequence that stars cannot pass directly from libration about R_1 to libration about R_2, and vice versa. There is no direct exchange of stars from one ring to the other. Stars from R_1 pass straight across the trapping region and end up untrapped, their eccentricities increased and rotating in the opposite sense.

The bar can also grow or fade in strength. The effects of such changes are equivalent to changes in the pattern speed. This is because the capture probability (3.25) depends only on the parameter λ. When λ increases, the numbers of librators and prograde rotators increase at the expense of the retrograde rotators. When λ decreases, the situation is reversed. From the definition (3.17), we see that λ increases if

$$\frac{-\dot{\Omega}_{\rm p}}{2|D_1|(J_{\rm r}-J_{\rm circ})} - \frac{\dot{A}_2}{3A_2} + \frac{\dot{\Omega}_{\rm p}D_2}{3|D_1|^3} > 0, \tag{3.26}$$

where $D_2 = \partial^2\Omega_{\rm p}/\partial J_{\rm s}^2$. The final term on the left-hand side of (3.26) is of higher order than the remaining two and may be neglected. So, we deduce that increasing the pattern speed $\Omega_{\rm p}$ or the bar strength A_2 both cause λ to diminish. Notice this gives a seemingly paradoxical result. As the bar grows, the numbers of trapped stars diminish! Normally, we expect growth of a potential well to enhance the probability of capture. This does not happen here because the U-point geometry tightly constrains the possible change in the phase space area of the trapped stars. So, if the bar is speeding up or increasing in strength, both the rings fade. Conversely, if the bar is slowing down or dissolving, both the rings grow.

There is one further deduction we can make. The capture probability (3.25) is a monotonic decreasing function of λ. So, for strong bars, the aligned outer ring is expected to be the most prominent. For weak bars, the anti-aligned ring is the dominant one. Although the sample is admittedly small, this appears to be borne out by a visual examination of figure 5 of Buta (1986). In the more weakly barred galaxies NGC 1291 and A0621.9-3211, the anti-aligned ring is more

conspicuous, whereas in the more strongly barred galaxy A1056.3-4619, the aligned ring is the brightest. As the observational evidence is suggestive rather than convincing, it would be interesting to test this prediction with numerical simulations.

3.3 3.3 Capture Probabilities at Non-Singular Points along the Envelope

In the previous examples, the scaling means that changes in pattern speed and amplitude are coupled. At a general point on the envelope, where the gradient term in (2.11) is less important, we have to consider their variations independently.

A rotating star can be captured into libration when the envelope of the section changes shape. Let us first consider the case when the trapping region is both moving and growing, but the lobe of the separatrix is symmetric. The Hamiltonian is

$$H = \tfrac{1}{2} D_1 \hat{J}^2 - A_2(1+\alpha t)\cos 2w, \tag{3.27}$$

where $\hat{J} = J - J_r(t)$ is the action measured with respect to the point of exact resonance. The amplitude A_2 is taken as positive without loss of generality, but the inertial response D_1 may have either sign. The parameter α describes the steady expansion of the envelope. The resonant action is also assumed to be changing slowly and linearly with time like

$$J_{\rm r}(t) = J_{\rm r}(0) - \beta t. \tag{3.28}$$

This implies that the pattern speed is slowing down like

$$\dot{\Omega}_{\rm p} = \dot{J}_{\rm s} \frac{\partial \Omega_{\rm p}}{\partial J_{\rm s}} = -\beta D_1. \tag{3.29}$$

The equations of motion are

$$\dot{J} = -2A_2 \sin 2w, \qquad \dot{w} = D_1(J - J_{\rm r}(0) + \beta t). \tag{3.30}$$

For the moment, both α and β are assumed small so adiabatic theory holds.

The separatrix lobe (see Fig. 8) moves downwards and changes in size. So, the regions P (corresponding to prograde rotators) and T (trapped orbits) increase in size, whereas the region R (retrograde rotators) diminishes. Initially, the separatrix lobe has an area equal to $8|A_2/D_1|^{1/2}$. The change in this area is just

$$\frac{dS_{\rm trap}}{dt} = 4\alpha \left| \frac{A_2}{D_1} \right|^{1/2}. \tag{3.31}$$

The change in the area P has two contributions. The first term describes the increase due to the shifting potential well. The second term is the diminuition caused by the encroachment of the separatrix lobe T. This gives the formula

$$\frac{dS_{\rm prog}}{dt} = \pi\beta - \tfrac{1}{2}\frac{dS_{\rm trap}}{dt}. \tag{3.32}$$

Using (3.11), the capture probability is

$$P = \frac{2}{1 + \frac{\pi}{2}\frac{\beta}{\alpha}\left|\frac{D_1}{A_2}\right|^{1/2}}. \tag{3.33}$$

If β is negative, then the region T (see Fig. 8) moves upward. Now, regions R and T increase in size, whereas P shrinks.

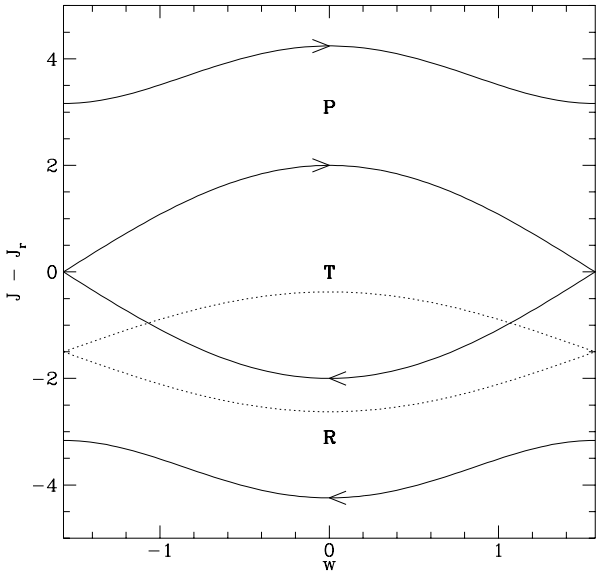

Figure 8. A snapshot of phase space corresponding to the Hamiltonian (3.27). The plot shows contours of constant energy in the action-angle plane (J, w). The separatrix lobe (marked T) is moving down the diagram as well as changing in size. The region R (retrograde rotators) is shrinking, while the region P (prograde rotators) is expanding. The position of the separatrix lobe at a later time – when it has moved and changed shape – is shown in the dotted line.

The formula (3.33) then gives the probability of capture of a prograde rotator.

More realistically, we must deal with cases where the envelope width and the inertia both depend on the action. In this case, the Hamiltonian is

$$H = \tfrac{1}{2} D_1 \hat{J}^2 + \tfrac{1}{6} D_2 \hat{J}^3 - (A_2 + B_2 \hat{J})(1+\alpha t)\cos 2w, \tag{3.34}$$

where $\hat{J} = J - J_r(t)$. Now, the separatrix lobe is asymmetric, as the unstable fixed point is displaced from the stable fixed point by $2A_2/D_1$ in action. The capture probability can be deduced by perturbation methods when D_2/D_1 and B_2/A_2 are small. We find:

$$P = \frac{2}{1 + \frac{\pi}{2}K}, \tag{3.35}$$

where

$$K = \frac{\beta}{\alpha}\left|\frac{D_1}{A_2}\right|^{1/2} \frac{1}{1 - \frac{\beta}{\alpha}(\frac{B_2}{A_2} - \frac{D_2}{D_1})} - \frac{3B_2D_1 - D_2A_2}{6|A_2D_1|^{3/2}}. \tag{3.36}$$

Tremaine & Weinberg (1984) have already examined the case when the potential well is moving but of fixed amplitude. Our formula (3.35) reduces to theirs in the limit $\alpha \to 0$. If D_2 is negative, the equiaction section becomes flatter as we move towards increasing angular momentum. So, if the well is moving towards high angular momentum, then the capture probability is enhanced. We can see this in two ways. As the section becomes flatter, the breadth in angular momentum of the trapping region has been increased. Equivalently, there is a smaller dispersion in resonant frequency across the section so that outlying orbits are more

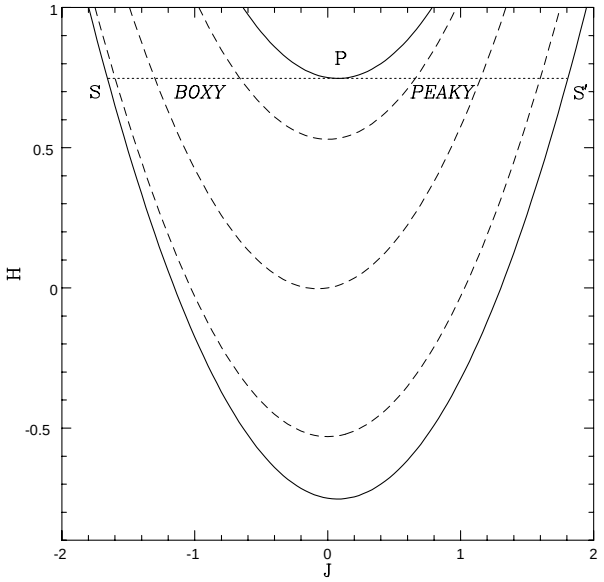

Figure 9. An equiaction section corresponding to the model Hamiltonian (3.39). The extra harmonic term leads to a boxy well when $\hat{J} < 0$ and a peaky well when $\hat{J} > 0$. The bunching of the inner lines show that the action of the branch SP is reduced, whereas that of the branch PS$'$ is increased. This explains the enhanced capture of the boxy well.

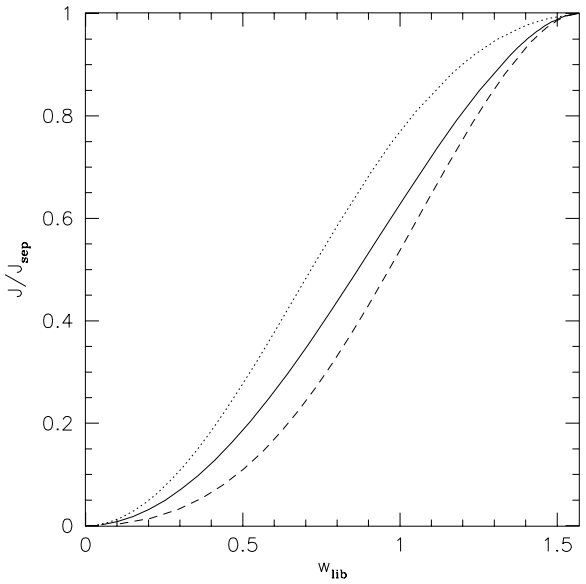

Figure 10. After capture, the star falls deeper into the well. The angular amplitude of libration $w_{\rm lib}$ is plotted against the normalised action $J/J_{\rm sep}$. The unbroken line is the $m = 2$ harmonic well. The dashed line is boxier ($A_4 = -0.20$) and the dotted line is peakier ($A_4 = 0.20$).

readily trapped. If B_2/A_2 is positive (and the well is moving towards increasing angular momentum), capture is made more likely as we are moving to a region of the section of greater width. In terms of the asymmetry of the separatrix lobe, it helps to have the larger lobe in the forward direction of the moving well.

The competition between terms in (3.36) again makes clear that a growing instability need not be accompanied by a monotonic growth in the membership of each resonant family. In other words, although the growth of the well aids capture, this can be offset by a movement of the resonance to a pattern speed (and hence orbital shape) in which the orbit experiences a smaller averaged potential. When the pattern speed changes, the periodic orbit deduced from (3.30) is actually offset from the bar potential by $\frac{1}{2}\,\mathrm{asin}(\beta/(2A_2))$. This is the means by which angular momentum is transferred between the periodic orbit and the well. This has the following interesting consequence. Suppose a bar to be composed of periodic orbits or boxes of small librational amplitude. In a steady state, the orbits are aligned and mutually provide the potential in which they sit. When the bar is decelerated at a rate $\dot{\Omega}_{\rm p}$, then we can anticipate a shear in the orientation of the orbits – since $D_1 A_2$ is different for each periodic orbit. Indeed, this can even lead to escape when $D_1 A_2$ is small. If the perturbation is like a pure quadrupole, this condition may be best satisfied towards the centre of galaxies or at the end of the bar.

3.4 3.4 Refinements

The formulae presented in the previous sections employed approximations to the Hamiltonian which we now relax. Here, we investigate the effects of (1) the deviation of the section width from the canonical form, (2) additional harmonics in the perturbation potential and (3) spiral waves.

Examination of the exact sections at inner and outer Lindblad resonance shows that the U-point approximation is valid in a region very close to the circular orbit. As this tip constricts, we can use the Hamiltonian:

$$\tilde{H} = \tilde{J}^2 - 2\lambda\tilde{J} - 2(2\tilde{J})^{1/2}(1 - \epsilon\tilde{J})\cos\tilde{w}, \qquad (3.37)$$

which incorporates the contribution from the next order eccentricity term. The problem now depends on two parameters and does not possess the simple scaling it had previously, which allowed us to consider pattern speed and growth changes as equivalent problems. What happens to the capture probability as a steady resonance sweeps past? It now becomes:

$$P = P_0(x_\star) + \epsilon\frac{\pi(8 - 5x_\star^3)}{4x_\star(x_\star^3 - 1)^{1/2}(\,\mathrm{asin}(x_\star^{-3/2}) + \pi/2)^2}. \qquad (3.38)$$

Here, the first term $P_0(x_\star)$ is the original capture probability (3.25). A sketch of the derivation of the second term is given in Appendix B, while $x_\star$ is defined in terms of the action of the unstable fixed point by (3.23). This is the same as used in Section 3.2, but of course the position of the unstable fixed point itself has moved in the perturbed problem. Note that $x_\star > 1 + 2\epsilon$, so that the singularity in the second term in (3.38) never occurs in physical applications where the tip constricts. The probability of capture close to a U-point can be either increased (if $x_\star < 2/5^{1/3}$) or decreased (if $x_\star > 2/5^{1/3}$), assuming ϵ is positive. When $x_\star$ is large, the width of the envelope of the section becomes more uniform and the phase area of the trapped orbits changes more slowly. When $x_\star$ is small, the unstable fixed point lies close to the tip. The perturbing term has a larger relative influence on shrinking

the area near the tip than the area of trapped orbits – and so the capture probability is increased.

More serious, perhaps, is the neglect of higher harmonic terms. This was already clear in the analysis of the Pluto-Neptune system in Section 2.3. As the perturbation grows in size or the orbit becomes more eccentric, the influence of the higher harmonics becomes more important. This can manifest itself in two ways – first, by changing the capture probability, and second, by modifying the response density contributed by the captured star. The effect of the harmonics is different at the three régimes of the equiaction section. The simplest régime to consider is at a general point on the section, where the Hamiltonian may be approximated by

$$H = \tfrac{1}{2}D_1\hat{J}^2 - \Big[A_2\cos 2w + A_4\hat{J}\cos 4w\Big], \tag{3.39}$$

where A_4 is assumed small and positive. The corresponding section is illustrated in Fig. 9. The capture probability – which would vanish in the absence of the higher harmonic term – is now

$$P = \frac{16}{3\pi}\frac{A_4}{|A_2D_1|^{1/2}}, \qquad A_4D_1 > 0, \tag{3.40}$$

when the well is moved towards the boxy part of the section ($\hat{J} < 0$). The probability remains zero when the well is moved in the opposite direction – indeed, now trapped stars seep out of the well. This may be understood on recalling the result of Section 3.3, namely that capture is enhanced by having the larger lobe in the forward direction of the moving well. Armed with this result, we may be tempted to believe that boxy wells always aid capture. This is not the case, as we shall now show. At the U-point, the second harmonic gives a contribution that goes like the square of the eccentricity. So, the U-point Hamiltonian is modified to:

$$\tilde{H} = \tilde{J}^2 - 2\lambda\tilde{J} - 2(2\tilde{J})^{1/2}\cos\tilde{w} - \mu\tilde{J}\cos 2\tilde{w}, \tag{3.41}$$

which effectively introduces an octopole into the bisymmetric wave. The calculation is outlined in Appendix B and the result for the capture probability is:

$$P = P_0(x_\star) + \mu\frac{\pi x_\star(x_\star^3-1)^{1/2}}{6(\,\mathrm{asin}(x_\star^{-3/2}) + \pi/2)^2}. \tag{3.42}$$

Surprisingly, when the well is sharpened ($\mu > 0$), the probability of capture is enhanced.

The effects of the extra harmonic term on capture can therefore be quite subtle. Let us now turn to our second point of how quickly a captured star sinks into the well. We take the Hamiltonian to be a modified form of (3.27)

$$H = \tfrac{1}{2}D_1\hat{J}^2 - \Big[A_2\cos 2w + A_4\cos 4w\Big]. \tag{3.43}$$

After capture, the star descends deeper into the well. The action of its new libration is again adiabatically invariant. This can be exploited to give a rough way of assessing when its response density becomes supportive of the trapping potential. In Fig. 10, the angular amplitude of libration $w_{\rm lib}$ is plotted against the action of the orbit normalised to the action of the separatrix $J/J_{\rm sep}$. The unbroken line refers to a pure $m = 2$ harmonic well, the dashed and dotted lines to boxier and peakier wells respectively. The peakier well ingests the star more quickly. The figure makes clear the relative change in action needed for the star to reinforce the perturbation well.

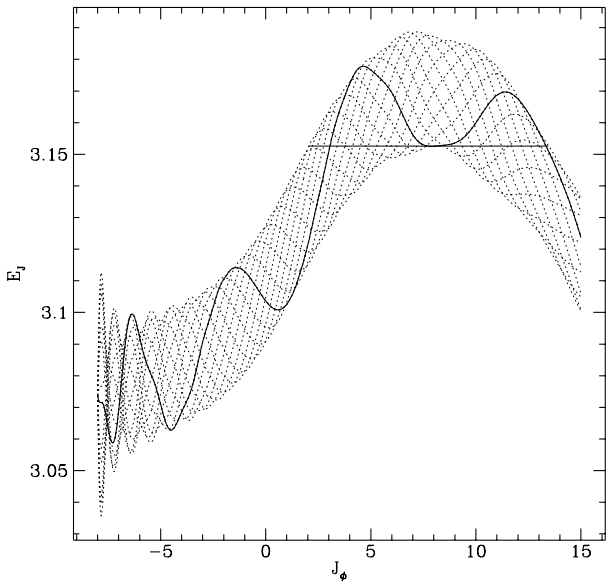

Figure 11. An equiaction section for a tightly wound spiral wave. The lines representing the values of the Jacobi integral at constant azimuth are shown in dotted lines – one is highlighted for clarity. The solid horizontal line is the separatrix. Interestingly, the separatrix now corresponds to a libration with amplitude *greater* than $\pi/2$. [The axisymmetric model used is the cored Mestel disk of Fig. 3. It is subjected to a logarithmic spiral perturbation with $m = 2$ and radial wave number $\alpha \sim 17$. This corresponds to a pitch angle of $\sim 83^\circ$, so that the spiral is tight].

Spiral waves change the section in two ways. First, the lines of constant slow angle now oscillate within the envelope. Second, the spiral wave effectively shears the potential in annuli so that the average potential has to be re-computed for each periodic orbit. It is not hard to see that the first change within an envelope of fixed shape leaves the capture probability formulae unaltered. The only modifications we need to consider are due to the second. The barred potential of Fig. 3 is replaced by a tightly wound logarithmic spiral in Fig. 11, viz;

$$\psi_{\rm p} = \epsilon\frac{R^2}{\tilde{R}_c^2 + R^2}\cos(m\phi - \alpha\log r). \tag{3.44}$$

The spiral wave has removed the X-points and – as we shall see in Section 4.2 – this permits angular momentum transport throughout the section. The Hamiltonian close to exact resonance may be written as

$$H = \tfrac{1}{2}D_1\hat{J}^2 - A_m\cos m(w - \lambda\hat{J}), \tag{3.45}$$

where λ is a measure of the spirality and strictly speaking depends on the fast action $J_{\rm f}$. In Fig. 11, the highlighted line has a positive curvature near the position of exact resonance, whilst the envelope of the section has negative curvature. This is characteristic of strong spirality and happens whenever $m|\lambda^2A_m/D_1|^{1/2} > 1$. There is no distinction between trailing and leading spiral waves as far as capture and escape are concerned.

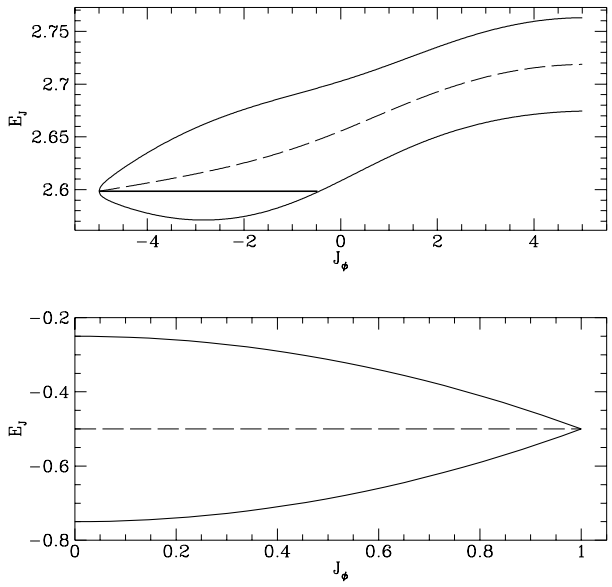

Figure 12. The upper equiaction section shows the negative angular momentum branch for the corotation resonance. The bold horizontal line corresponds to a librating orbit that almost reaches to the galactic centre. The overall flatness of the section means that small disturbances can lead to large changes in orbital shape. The lower panel is an equiaction section for Keplerian ellipses subjected to a stationary planar quadrupole. The section is remarkable for its flatness. The central seam is horizontal manifesting the degeneracy of the Keplerian orbits.

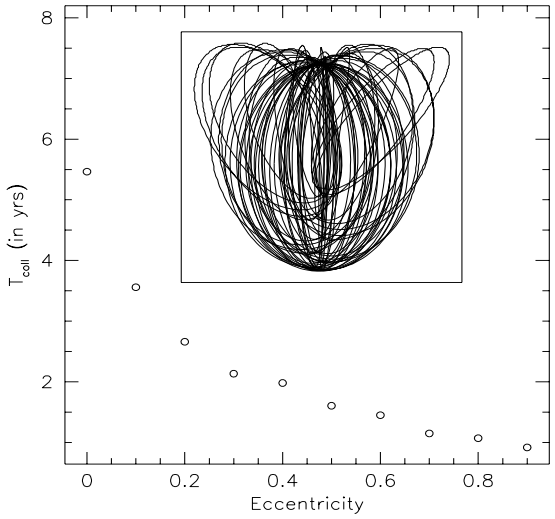

Figure 13. The two panels show how the collision time $T_{\rm coll}$ of a lunar orbit varies with eccentricity and orbital inclination. The inset to the first panel shows the lunar orbit in the Lidov experiment. The inset to the second panel depicts the orbital geometry.

4 4 APPLICATIONS

4.1 4.1 Large Eccentricity Changes

The equiaction section allows us to find the periodic orbits on which cold gas settles. As the periodic orbit increases in eccentricity, it develops self-intersections and can no longer support a steady gas stream. However, this is not true of one orbital family, namely the $(\ell = 0, m = 1)$ family. All the orbits belonging to this sequence are not self-intersecting. In principle, gas could be shipped right to the galactic centre through a continuous series of periodic orbits. This provides one possible mechanism for fuelling the nucleus with counter-rotating gas from large radii. Of course, streams of counter-rotating gas are common in spirals and S0s (e.g., Bertola, Buson & Zeilinger 1992). This mechanism is viable if the angular momentum of the periodic orbit changes markedly under moderate disturbances. This is true of any resonance possessing a flat section. An example of this is obvious from Fig. 1, where the $(\ell = 0, m = 1)$ fast action tangents are nearly parallel to the resonance lines. This situation persists over a broad range of pattern speeds. The $m = 1$ disturbance couples most strongly to this set of resonant orbits and the U-point at its tip ensures that there are always nearly circular periodic orbits. In an $m = 2$ disturbance, the tip becomes a V-point, generally without an associated stable periodic orbit for the gas to sit on. The only stable periodic orbit is that associated with the moving resonance and this is capable of moving from circular to radial orbits. Stars, on the other hand, can undergo the large scale shape changes through libration alone, a typical example of which is indicated on Fig. 12. This shows the negative angular momentum branch for the co-rotation $(\ell = 0, m = 1)$ resonance. The axisymmetric model is the cored Mestel disc subject to the disturbance

$$\psi_{\rm p} = \epsilon \frac{R}{R^3 + a^3} \cos m\phi. \tag{4.1}$$

As indicated by the bold horizontal line on the upper panel of Fig. 12, the libration swings from circular to very nearly radial for some orbits.

Close to the galactic centre, if a massive black hole is present, the gravity field is nearly Keplerian. The gas can

follow the closed periodic elliptical orbits. In order to direct gas and stars onto the hole, a mechanism of increasing the eccentricity of the orbit is again required. A tidal field inclined at an angle to the orbital plane is one possibility. We can estimate the timescale on which the mechanism proceeds as follows. Let us consider the Hamiltonian

$$H = \tfrac{1}{2} D_2 \hat{J}^2 - A_2(\hat{J}, t) \cos 2w. \tag{4.2}$$

For the Kepler potential, D_2 vanishes for the $(\ell = 0, m = 1)$ resonance. The amplitude can be taken as (c.f., the lower panel of Fig. 12)

$$A(\hat{J}, t) = a(t)\Big[1 - \frac{\hat{J}^2}{\hat{J}^2_{\rm circ}}\Big], \tag{4.3}$$

where $a(t)$ is an arbitrary function of time. Let us choose the normalisation so that the circular orbit has unit action, i.e., $\hat{J}_{\rm circ} = 1$. The trajectories of the equations of motion are independent of the function $a(t)$, namely

$$\cos 2w \propto \frac{1}{1 - \hat{J}^2}. \tag{4.4}$$

A particularly simple case is when $a(t)$ is just a constant, say A. Then, gas starting on an orbit with action-angle coordinates $(\hat{J}_0, w_0)$ loses all its angular momentum in the time

$$T_{\rm coll} = \frac{1}{2A} \int_0^{\hat{J}_0} \frac{d\,\hat{J}}{([1 - \hat{J}^2]^2 - [1 - \hat{J}_0^2]^2 \cos^2 2w_0)^{1/2}}. \tag{4.5}$$

This expression can be recast as an elliptic integral, but it is easy to work out numerically as needed. If the gas starts out on exactly circular orbit, then it can never lose all its angular momentum, but small eccentricities can be amplified quickly. In his fascinating book *Huygens & Barrow, Newton & Hooke*, Arnold (1990) briefly reported an observation made by Lidov (1963). Lidov discovered that if the orbit of the Moon is turned through 90°, its eccentricity increases so rapidly under the action of the tidal forces of the Sun that it collides with the Earth in four years! An order-of-magnitude confirmation is provided by (4.5) with the constant A roughly equal to the tidal potential due to to the Sun, i.e., $A \sim GM_\odot r^2/R^3$. Here, R of course refers to the Earth-Sun distance and r to the Earth-Moon distance. Taking the eccentricity of the Moon's orbit at the present day as 0.055 (Allen 1973), then the time taken for collision with the Earth $T_{\rm coll}$ is calculated by (4.5) as ~ 3.7 years.

To investigate this problem further, the equations of motion of the Moon in axes rotating with the Earth and under the action of the solar tides

$$\begin{aligned}
\ddot{x} &= -\frac{GM_\oplus x}{r^3} + \frac{3GM_\odot x}{R^3} + 2\Omega\dot{y}, \\
\ddot{y} &= -\frac{GM_\oplus y}{r^3} - 2\Omega\dot{x}, \\
\ddot{z} &= -\frac{GM_\oplus z}{r^3} - \frac{GM_\odot z}{R^3}.
\end{aligned} \tag{4.6}$$

were integrated numerically by fourth-order Runge-Kutta methods. Here, the x-axis points towards the Sun, and the z-axis points out of the plane of the ecliptic. Fig. 13 shows the results of these integrations, in which the Moon always starts off on the z-axis at apocentre. Coriolis force causes the orbital plane to precess. The conserved perturbation potential that is appropriate here is an azimuthal mean of the tidal potential felt around the figure of the orbit. In the Lidov experiment (shown as an inset), this means that the line of apsides of the orbit eventually settles to a torquing angle $\theta_{\rm t}$ of $\sim 51°$ (in contrast to the simple Hamiltonian (4.2), where $\theta_{\rm t} = 45°$). The final torquing angle for arbitrary eccentricity may be deduced from the conserved potential as

$$\cos 2\theta_{\rm t} = \tfrac{1}{5}(6e^2 - 1). \tag{4.7}$$

The maximal torque occurs when $\theta_{\rm t} = 45°$ so that the eccentricity curve flattens out. When the orbital plane is inclined, the collision time $T_{\rm coll}$ increases dramatically, and this limits the range of orbits that can be tidally elongated. This mechanism may have interesting applications in the central regions of galaxies dominated by black holes, where the potential is nearly Keplerian. Tidal forces, perhaps caused by a sinking object, can drive orbiting stars into the hole. Another application is to the survival of high inclination comets and asteroids, where indeed this instability has already been discovered anew (e.g., Kozai 1980; Stagg & Bailey 1989).

4.2 4.2 Modes

A disturbance changes the angular momentum of the stars in two ways. First, it may capture a star and carry that trapped star as it moves. Otherwise, it will *flip* the stars that it encounters from one sense of rotation to the other. The angular momentum transferred in the second process depends upon the speed of transition. Tremaine & Weinberg (1984) investigated this for non-singular points along the envelope. Here, we supplement their calculations with those appropriate to orbits of low eccentricity close to a U-point and general orbits near X-points.

Now let us imagine a disturbance at inner Lindblad resonance, the pattern speed of which is slowly decreasing. As the disturbance sweeps across the section, it encounters first the low phase density tail of this distribution. If we assume the amplitude of the wave to be steady, then each star is flipped and none are caught (see Section 3.2). This angular momentum jump decreases as we approach the tip of the section, but all stars are shifted and so, after the disturbance has passed, a hole has opened up with a sharp edge and the distribution has lost the orbits that were originally very near to circular. In addition, the tail of the distribution has been distended. For example, suppose we have a warm exponential disk with a radial scale-length $1/\alpha$ and a central velocity dispersion σ_0. If the disk has a completely flat rotation curve ($v_{\rm circ} = 1$), then the potential in the plane is that of Mestel (1963). If the velocity dispersion is also exponentially declining, then the distribution function has the form (Newton 1986; Binney 1987; Kuijken & Tremaine 1991)

$$f(J_R, J_\phi) = f_0 \exp\Big[-\sigma_0^{-2} \exp(\alpha J_\phi) \kappa J_R\Big], \tag{4.8}$$

where f_0 is independent of the velocities. Along the section, this becomes

$$f(J_{\rm f}, J_{\rm s}) = f_0 \exp\Big[-\sqrt{2}\sigma_0^{-2} \exp(\alpha J_{\rm s})(\frac{J_{\rm f}}{J_{\rm s}} \pm \frac{1}{2})\Big]. \tag{4.9}$$

Here, the negative sign is appropriate for ILR, the positive sign for OLR. For a flat rotation curve, the Hamiltonian for

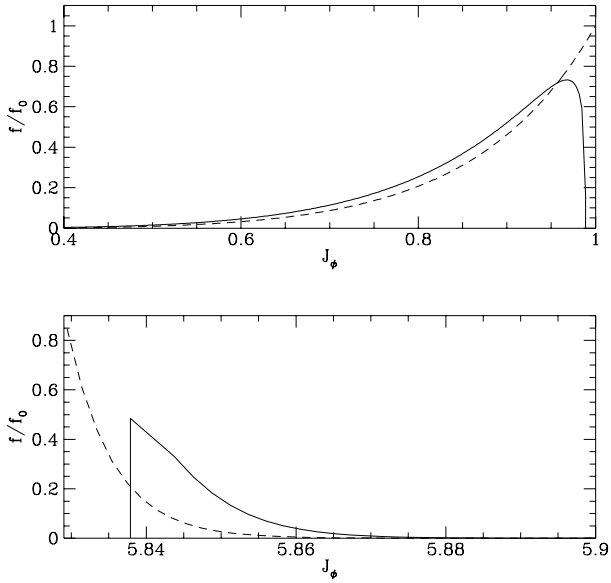

Figure 14. The upper and lower panels show the distribution function of the warm exponential disk at inner and outer Lindblad resonance respectively. In each case, the distribution function is shown before (in dashed line) and after (in unbroken line) a wave sweeps across the equiaction section. The disturbance heats the disk and opens up a hole in the distribution function corresponding to the missing circular orbits. [The upper panel is drawn with $J_{\rm f} = 0.5$, the lower panel with $J_{\rm f} = -2.9$ in units in which $\sigma_0 = 1/4$ and $v_0 = \alpha = 1$.]

epicyclic orbits may be approximated by

$$H = \frac{1}{2} + \log J_\phi + \sqrt{2}\frac{J_R}{J_\phi} - \frac{11 J_R^2}{12 J_\phi^2}. \tag{4.10}$$

from which the inertial response D_1 at both ILR and OLR is negative. This can also be deduced by inspection of the lower panel of Fig. 1. The distribution function is so steep that we assume for simplicity that D_1 is the same for all the stars within each section and the Hamiltonian can (with a scaling) be brought into the form (3.16). To work out the flip experienced by each star, we match its initial action to the action along the incident branch of the separatrix. The corresponding jump is then just the phase area of the separatrix lobe. As before, let the scaled action of the unstable fixed point P at the moment of flipping be $x_\star^2/2$. The phase area between any orbit and the circular orbit at the end of the tip is $\pi|J_{\rm circ} - J|$. This is scaled and matched to the area under the inner separatrix branch

$$S_{\rm ret} = (\frac{\pi}{2} - \,{\rm asin}(x_\star^{-3/2}))(x_\star^2 + \frac{2}{x_\star}) - \frac{3(x_\star^3 - 1)^{1/2}}{x_\star}. \tag{4.11}$$

The flip F will then be

$$F = 2\Big[(x_\star^2 + \frac{2}{x_\star})\,{\rm asin}(x_\star^{-3/2}) + \frac{3(x_\star^3 - 1)^{1/2}}{x_\star}\Big]. \tag{4.12}$$

The final area under the phase curve $S_{\rm prog}$ is just the initial area plus the flip, or

$$S_{\rm prog} = F + S_{\rm ret} = \pi\Big[x_\star^2 + \frac{2}{x_\star}\Big] - S_{\rm ret}. \tag{4.13}$$

Figure 15. The creation of a notch in the distribution function. The upper panel highlights two strips of phase. The dark phase is denser. After passage across the separatrix, stars from these strips are partitioned between two populations as shown in the second panel. The region of lower phase density now lies between two high density strips. (Here, the phase density is stratified on lines of constant $E_{\rm J}$. The equiaction section does not justly represent phase areas, but for pictorial convenience, we have drawn each strip with a constant strip-averaged phase density).

When the disturbance has moved far away, this is – once unscaled – the new slow action or angular momentum $J_\phi^{\rm n}$ of the star. The final coarse–grained distribution function along the section is

$$f_{\rm coarse}(J_R, J_\phi^{\rm n}) = f(J_R, J_\phi)\frac{{\rm d}J_\phi}{{\rm d}J_\phi^{\rm n}}, \tag{4.14}$$

where the Jacobian is

$$\frac{{\rm d}J_\phi}{{\rm d}J_\phi^{\rm n}} = \frac{\frac{\pi}{2} - \,{\rm asin}(x_\star^{-3/2})}{\frac{\pi}{2} + \,{\rm asin}(x_\star^{-3/2})}. \tag{4.15}$$

The distribution function is coarse–grained because "air" has become mixed up with the phase as the well passes and the phase area deflates. This point is made clearly by Sridhar & Touma (1996), who performed a related calculation on vertical heating of stars in a galactic disk by sweeping resonances. Fig. 14 shows the initial (dashed line) and final (unbroken line) distribution functions for the warm exponential disk. The upper panel refers to ILR, the lower panel to OLR. In each case, the flips get smaller towards the tip and the last flip creates a hole with width W

$$W = \frac{3\pi}{2^{1/3}}\Big|\frac{A_2}{D_1}\Big|^{2/3}. \tag{4.16}$$

The hole has been advected by the well from a region of zero phase density and deposited at the end of the tip entirely vacating the near-circular orbits. If the disturbance moves in the opposite direction, *into* the section, a different redistribution of phase occurs. The section bends as shown in Fig. 15 and the phase settles into horizontal layers until the

appearance of the separatrix. Layers above the separatrix at this point will then be processed in turn. A portion of the phase will move into the main well and a portion will flip in accordance with the capture probability. As the diagram makes clear, a notch is created in the distribution function. Adiabatic transfer of phase is one mechanism for creating inverted populations – in the sense that the phase space density gradients have their sign changed. This is true here but the phase density is still most concentrated about the two periodic orbits. Such holes and notches in the distribution function are well-known sites of instability (Toomre 1981; Sellwood & Kahn 1991).

The holes lead to a systematic gain in angular momentum at OLR, and a loss at ILR. This is similar to, but not identical with, the effect discovered by Lynden-Bell & Kalnajs (1972). Their famous formula for angular momentum transport applies to infinitesimally small waves, so small in fact that no star completes a traverse of the separatrix. Consequently, the issue of capture and escape is irrelevant to their calculation as is suggested by the absence of terms involving the gradient of the amplitude of the disturbance, i.e.,

$$\dot{J}_\phi = \frac{-1}{8\pi}\int dJ_{\rm f}\int dJ_{\rm s} m^2 \frac{\partial F}{\partial J_{\rm s}} A_m^2 \delta(m\Omega_{\rm p} - m\Omega - \ell\kappa). \quad (4.17)$$

What is relevant, however, are the amounts of phase just entering into libration near the two branches of the separatrix and this is manifest in the gradient of the distribution function in (4.17). In the flipping mechanism, the hole displaces phase around itself, irrespective of density gradients. A nice picture to have in mind is of a bubble in a spirit level.

The shunting mechanism relies on there being no capture and so the hole remains empty. It is interesting to see if this situation persists when the amplitude of the perturbation is turned on more quickly. To this end, Monte Carlo simulations were performed with the equations of motion derived from the Hamiltonian (3.16) with a Gaussian turn-off

$$\lambda = \lambda_0 \exp(-at^2), \quad (4.18)$$

From (3.17), turning λ off is equivalent to increasing the amplitude of the disturbance. The constant a determines the speed of separatrix crossing. The results are shown in Fig. 16 for two different values of λ_0. The probability of flipping remains unity as we move out of the adiabatic régime. The dip has an interesting explanation. The turn-off law has an inflection point at $t = (2a)^{-1/2}$. If stars make their inward crossing of the separatrix just before this time, they can then lose more energy than they gain on the outward crossing. This is a deviation from adiabatic theory. Whilst subtleties of this kind should be observed, adiabatic invariants are – in the nice phrase of Alar Toomre – "very forgiving".

Since capture at a U-point even by a rapidly growing wave is hard, it would appear difficult to establish a density supporting population to build, for instance, a bar from near-circular ILR orbits. This difficulty can be circumvented by capture at frequencies above the ILR. In this case, the trapped family are the distorted circular orbits and, intriguingly, a negative inertial response now promotes a quick shedding of angular momentum and a density enhancing elongation of the orbits. This is illustrated on the equiaction sections shown in Fig. 17, where the curvature of the section in the negative

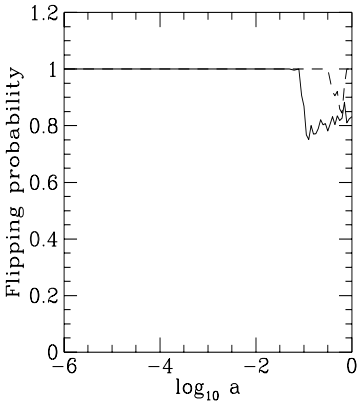

Figure 16. Monte Carlo simulations of the equations of motion at a U-point (3.16) subject to a slow turn-on of the trapping potential. In adiabatic theory, all the stars flip from prograde to retrograde rotation. The probability of flipping is plotted against the constant a. The larger the value of a, the faster the speed of separatrix crossing. Adiabatic theory is seen to hold good over nearly five orders of magnitude. (The full line refers to $\lambda_0 = 3$, the dashed line to $\lambda_0 = 16.5$).

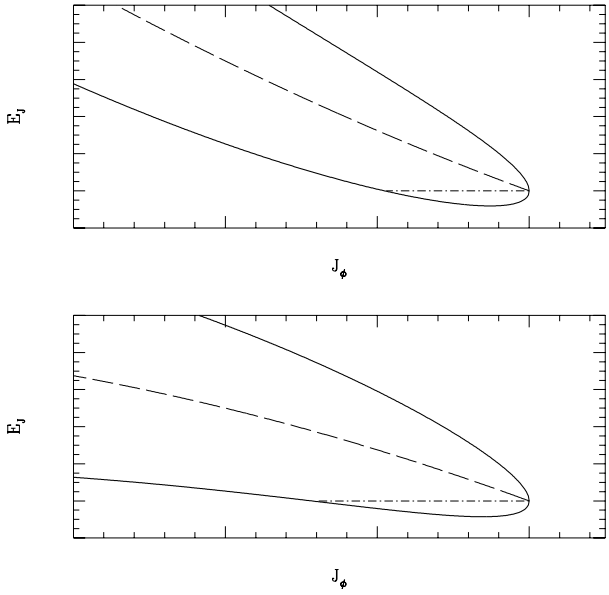

Figure 17. Equiaction sections for stars whose ILR frequencies are below that of the applied perturbation. The distorted circular orbits are trapped into libration below the pseudo-separatrix indicated by a dot-dashed line. In the upper panel, the stars possess positive inertial response, in the lower panel, negative. Capture into a potential reinforcing libration is now assisted by negative inertial response, the curvature of the section acting with the swelling of the envelope

inertial case acts with the swelling of the envelope.

The closing of the envelope at the U-point led to a hole in the distribution function. Similar behaviour occurs close to an X-point. If we consider the transition between the two main panels of Fig. 6, stars close to the X-point and above SP_1 are again dispatched into counter-rotation, with

their angular momentum flip diminishing the closer they are to the X-point. Eventually, the separatrix is replaced by a pseudo-separatrix. The advection of angular momentum is stopped at a stationary X-point. If the X-point is moving – as surely it is – then stars can be squeezed across, much like icing from an icing bag. The relative number of stars trapped into libration about P_1 or P_2 is once more determined by the growth rates of the phase space areas associated with the trapping region. When the pattern speed alone is changing, the trapping region around P_2 is essentially excluding phase, whereas that around P_1 is swallowing phase. Stationary X-points make the wave give up its bound angular momentum.

4.3 4.3 Figure Rotation and Triaxial Models

Analyses of images of galactic nuclei taken with the HST planetary camera have shown that the surface brightness distributions of early-type galaxies are almost always cusped (Lauer et al. 1996). For example, the surface brightness of the nearby S0 galaxy NGC 7547 is cusped in the inner 600 parsecs like R^{-1}. Although there is no difficulty in the sustenance of axisymmetric cusps (e.g., Evans 1994), the survival of triaxial cusps is a much more delicate matter. For a point perturber in a triaxial non-rotating galaxy, Gerhard & Binney (1985) computed the timescale on which a typical box orbit suffers a serious deflection. They concluded that box orbits with apocentres $\lesssim$ 1 kpc are disrupted over the course of a Hubble time. This process may cause the shape of the inner parts of galaxies to become axisymmetric. Schwarzschild and co-workers (Miralda-Escudé & Schwarzschild 1989; Lees & Schwarzschild 1992) have also suggested that strongly flattened triaxial figures with density cusps may not be able to persist. Recently, Merritt & Fridman (1995) presented numerical results on the existence of non-rotating triaxial galaxy models with cusps. Only for weak central cusps ($\rho \sim r^{-1}$) were they able to build equilibrium models, raising again the question of the existence of stationary triaxial galaxies with strong central cusps ($\rho \sim r^{-2}$). In this section, we suggest an answer to the question : does figure rotation aid the survival of triaxial models with central scatterers?

The upper and lower panels of Fig. 18 show equiaction sections in static and mildly rotating triaxial potentials. A typical box orbit is marked by a bold horizontal line in each case. B_1 and B_3 mark the points where the libration reaches the bottom of the well. At B_2, the libration finishes its swing. The dashed curve defines the opening angle of the fan. When the potential is static, the box orbit turns round in azimuth on the radial orbits ($J_\phi = 0$). When the potential is rotating, this turn-round occurs on an eccentric but non-radial orbit ($J_\phi \neq 0$). The upper and lower panels of Fig. 19 again refer to static and rotating triaxial potentials. In each case, the orbit produced by propelling a star from the same spot on the minor axis with the same speed is shown, together with the linear density across the waist. In the non-rotating case, this possesses cusps only at the waist's edge, but inner cusps appear when there is figure rotation. The inner cusp is brought closer to the centre by moving the point B_1 in Fig. 18 towards $J_\phi = 0$. This subtlety aside, the more striking change is that the waist of the box orbit has been broadened and the probability of hitting the centre reduced. Waist broadening by figure rotation will therefore assist the survival of triaxial galaxies with central scatterers.

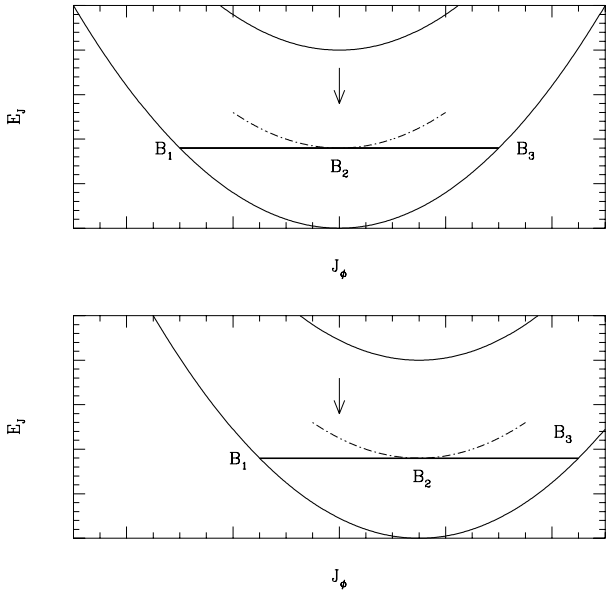

Figure 18. The upper panel shows an equiaction section at inner Lindblad resonance ($\ell = 1, m = 2$). The bold horizontal line represents a trapped box orbit in a galaxy with no figure rotation. The lower bounding curve of the section represents the trough of the well. So, B_1 and B_3 mark the points where the box orbit crosses the trough. The dot-dashed line is the potential at the slow angle w marking the amplitude of libration of the box. This occurs at B_2, which coincides with $J_\phi = 0$ (marked by an arrow). So, the box orbit is bounded by straight line segments. The lower panel shows the changes inflicted by rotation. The point B_2 is now offset from $J_\phi = 0$ and so the box orbit is no longer bounded by straight lines.

We can also use the theoretical methods of this paper to estimate the relative numbers of stars that are cast into the prograde and retrograde directions when a bar dissolves. This may be relevant to formation histories of galaxies like NGC 4550, which is built from two similar counter–streaming stellar components (Evans & Collett 1994). A bar will consist of stars in a laminate of sections, and the capture probability must be evaluated for each. In a strong bar, the curvature of the envelope dominates over the central seam, but in the final stages of dissolution or for weak bars, we can use the analysis of Section 3.3. For a non-rotating bar, we lose equally into the two streams. When there is rotation, the envelope of the section is thinner towards the tip. Mild rotation is represented in the lower panel of Fig. 18. The boxes are still very elongated and have a positive inertial response, like rods. We can estimate the relative size of the two streams as follows. The phase areas under the prograde and retrograde parts of the lobe are:

$$\begin{aligned} S_{\rm prog} &= 4\left|\frac{A_2}{D_1}\right|^{1/2} + \pi\frac{3B_2D_1 - D_2A_2}{3D_1^2}, \\ S_{\rm ret} &= 4\left|\frac{A_2}{D_1}\right|^{1/2} - \pi\frac{3B_2D_1 - D_2A_2}{3D_1^2}. \end{aligned} \tag{4.19}$$

A simple scale change of the envelope implies $\dot{B}_2 = \dot{A}_2 B_2/A_2$. The number of stars that escape into the two streams is proportional to the changes in the two areas

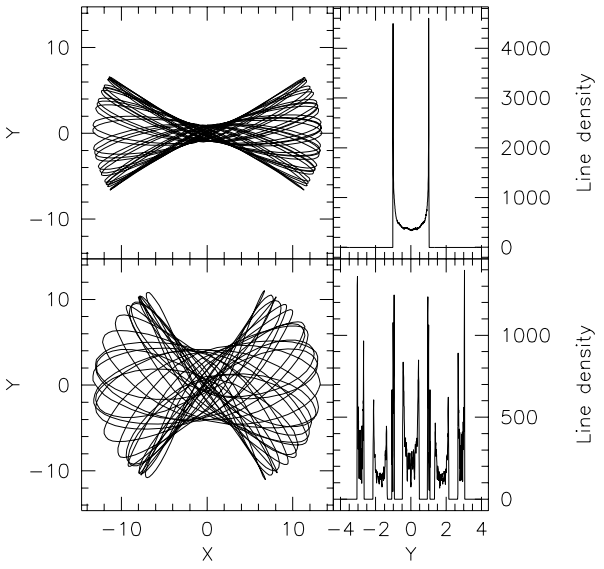

Figure 19. The upper two panels show a box orbit in the principal plane of a stationary triaxial potential, together with the orbital density across its waist. The two orbital density spikes correspond to the bounding straight line sections of the box orbit. The lower two panels show the same orbit in a triaxial potential with figure rotation. The box orbit is bounded by looping segments rather than straight lines. [The model used is the Binney potential with $q = .9$ and $v_0 = R_c = 1$. The orbits are both launched form the minor axis $(x = 0, y = 1)$ with $(v_x = 2, v_y = -.2)$. The pattern speed $\Omega_{\rm p} = 0$ in the former case and 0.015 in the latter.]

(4.19). We find that the streams are weighted $\frac{1}{2} + \alpha : \frac{1}{2} - \alpha$, with

$$\alpha = \frac{\pi}{12} \frac{(3D_1B_2 - D_2A_2)}{|D_1^3 A_2|^{1/2}}. \qquad (4.20)$$

Along an inner Lindblad section, the inertial response can change from positive near the radial orbits to negative for near-circular orbits (see the lower panel of Fig. 1). There is a point, then, at which D_1 vanishes and the above analysis is not valid. For a weak, fast rotating bar, we can return to the analysis of Section 3.2. In this case, stars are more bound when the amplitude drops. If the rule-of-thumb (4.20) is applied to the slow moving bar in the upper panel of Fig. 4, then the number of stars moving in the prograde sense is enhanced to ~ 60 per cent. This is by no means a small asymmetry, especially in view of the slowness of the bar. This suggests that it is possible to build markedly asymmetric counter-streams by break-up of a rapidly rotating bar.

5 5 CONCLUSIONS

This paper has shown how to calculate population changes caused by resonant escape and capture in a disk of stars. These processes depend on the shape of the effective potential well for orbital capture. Changes in the well are easy to picture on an equiaction section. For time-dependent problems, in particular, the equiaction section offers advantages over alternatives, such as Poincaré surfaces of sections. The main results of the paper are:

(1) There are barred galaxies with two outer rings of gas and stars (so-called $\rm R_1'R_2'$ galaxies). It is very difficult to transfer stars between the two outer rings in $\rm R_1'R_2'$ galaxies. Surprisingly, if the bar is decelerating or dissolving, both the rings can grow. If the bar is speeding up or increasing in strength, both the rings fade.

(2) Counter-rotating stars and gas are particularly susceptible to large eccentricity change. This mechanism could be important in channelling stars and gas towards the centres of galaxies. Tidal resonant forcing of highly inclined orbits around a central massive object will increase the likelihood of close encounters between the orbiting star and the object. So, in the centres of galaxies, tidal forces – perhaps caused by a sinking object – can drive orbiting stars onto a black hole.

(3) Resonances can create sharp holes and notches in the stellar distribution function, as well as high velocity tails, the width and shape of which we have explicitly calculated. The advection of angular momentum can be halted by the ocurrence of X-points (defined in section 2.2).

(4) Figure rotation will assist the survival of triaxial, cusped models by broadening the waists of box orbits. Moderate asymmetries in the populations of prograde and retrograde stars are produced by dissolving mildy rotating bars. A counterstreaming disk with, say, 60 per cent of stars moving in the prograde, 40 per cent in the retrograde direction is a likely end-point of the disruption.

ACKNOWLEDGMENTS

It is a pleasure to thank Donald Lynden-Bell, Pak-Li Chau, Alar Toomre, James Binney, David Earn and Christophe Pichon for useful conversations. JLC acknowledges financial support from PPARC (grant number GRJ 79454), while NWE is supported by the Royal Society. David Earn and Donald Lynden-Bell gave helpful and generous comments on the draft version of the paper. We thank Scott Tremaine and Norm Murray for drawing our attention to the work of Kozai and Bailey.

REFERENCES

Allen C. W., 1973, Astrophysical Quantities. The Athlone Press, London, chap. 7.
Arnold V. I., 1989, Mathematical Methods of Classical Mechanics. Springer-Verlag, Berlin, second edition, chap. 10
Arnold V. I., 1990, Huygens & Barrow, Newton & Hooke. Birkhäuser, Basel, p. 72
Athanassoula E., Bosma A., Créze M., Schwarz M. P., 1982, A&A, 107, 101
Athanassoula E., Bosma A., 1985, ARAA, 23, 147
Bertola F., Buson L. M., Zeilinger W. W., 1992, ApJ, 401, L79
Binney J. J., 1982, MNRAS, 201, 1
Binney J. J., Tremaine S. D., 1987, Galactic Dynamics. Princeton University Press, Princeton
Binney J. J., 1987, in Gilmore G., Carswell B., The Galaxy. Reidel, Dordrecht, p. 399
Borderies N, Goldreich P., 1984, Celest. Mech., 32, 127
Born M., 1927, The Mechanics of the Atom. G.Bell & Sons, London, chap. 4

Braun R., Walterbos R., Kennicutt R., 1995, Nature, 360, 442
Buta R., 1986, ApJS, 61, 609
Cary J. R., Escande D. F., Tennyson J. L., 1986, Phys. Rev. A, 34,4256
Ciri R., Bettoni D., Galletta G., 1995, Nature, 375, 661
Cohen C. J., Hubbard E. C., 1965, AJ, 70, 10
Collett J. L., 1995, Ph. D. thesis, Cambridge University, chaps. 2, 3
Contopoulos G., Papayannopoulos Th., 1980, A&A, 92, 33
Donner K. J., 1979, Ph. D. thesis, Cambridge University, chap. 6
Earn D. J. D., 1993, Ph. D. thesis, Cambridge University, chap. 3
Earn D. J. D., Lynden-Bell D., 1996, MNRAS, 278, 395
Evans N. W., 1994, MNRAS, 267, 333
Evans N. W., Collett J. L., 1994, ApJ, 420, L67
Gerhard O. E., Binney J. J., 1985, MNRAS, 216, 467
Goldreich P., 1965, MNRAS, 130, 159
Goldreich P., Tremaine S. D., 1981, ApJ, 243, 1062
Gutzwiller M. C., 1990, Chaos in Classical and Quantum Mechanics. Springer-Verlag, Berlin, chap. 7
Henrard J., 1982, Celest. Mech., 27, 3
Henrard J., 1993, Dynamics Reported 2. Springer-Verlag, Berlin, p. 117
Henrard J., Lemaître A., 1983, Icarus, 55, 482
Kalnajs A. J., 1973, Proc. Astron. Soc. Australia, 2, 174
Kalnajs A. J., 1977, ApJ, 212, 637
Kozai Y., 1980, Icarus, 41, 89
Kuijken K., Tremaine S.D., 1991, in Sundelius, B., Dynamics of Disc Galaxies. Göteborg University Press, Göteborg, p. 71
Landau L. D., Lifshitz E.M., 1969, Mechanics, Pergamon Press, Oxford, p. 134
Lauer T., et al., 1996, AJ, in press
Lees J., Schwarzschild M., ApJ, 384, 491
Lidov M. L., 1963, in Problems of Motion of Artificial Celestial Bodies. Akad. Nauk SSSR, Moscow, p 119 (in Russian)
Lynden-Bell D., Kalnajs A. J., 1972, MNRAS, 157, 1
Lynden-Bell D., 1973, in Dynamical Structure and Evolution of Stellar Systems. Geneva Observatory, Sauverny, p. 91
Malhotra R., 1993, Nat, 365, 819
Merritt D., Fridman T., 1996, ApJ, 460, 136
Mestel L., 1963, MNRAS, 126, 553
Miralda-Escudé J., Schwarzschild M., 1989, ApJ, 339, 752
Newton A., 1986, D. Phil. thesis, Oxford University
Peale S. J., 1976, ARAA, 14, 215
Sellwood J., Kahn F. D., 1991, MNRAS, 250, 278
Sridhar S., Touma J., 1996, MNRAS, 279, 1273
Stagg C., Bailey M., 1989, MNRAS, 241, 506
Tremaine S. D., Weinberg M., 1984, MNRAS, 209, 729
Toomre A., 1981, in Fall S. M., Lynden-Bell D., The Structure and Evolution of Normal Galaxies. Cambridge University Press, Cambridge, p. 111.
Yoder C., 1973, Ph. D. thesis, University of California, Santa Barbara
Yoder C., 1979, Celest. Mech., 19, 3

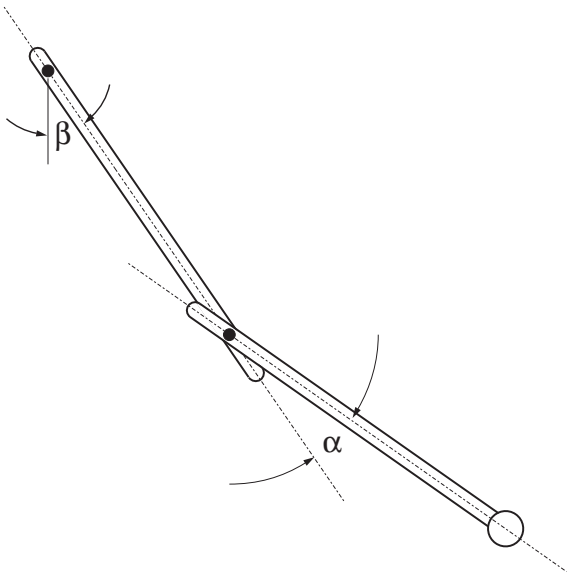

Figure 20. A picture of the jointed arm.

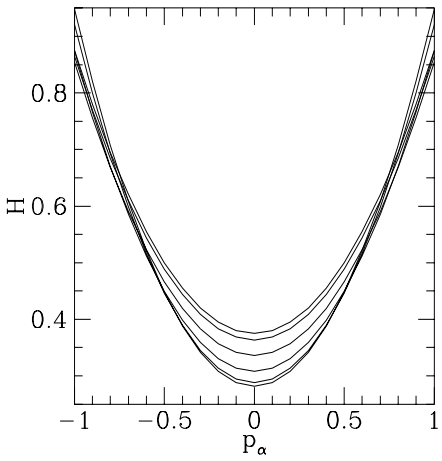

Figure 21. A plot of the energy integral (H) against the canonical momentum p_α for the arm at a fixed value of the canonical momentum p_β. This is analogous to the equiaction sections discussed in the main body of the paper. The lines are drawn at representative, equally spaced values of α between 0 and π. Trajectories on the section are horizontal lines bounded by the envelope.

6 APPENDIX A: THE JOINTED ARM

Fig. 20 depicts a simple mechanical system – a mass attached to a fixed pivot by a jointed arm. We suppose that all the inertia of the arm resides in that part attached to the fixed pivot. The Lagrangian of the system is just the kinetic energy, which we may write as

$$L = (\mu + 1)\dot{\beta}^2 + \dot{\alpha}\dot{\beta} + \frac{1}{2}\dot{\alpha}^2 + \dot{\beta}(\dot{\alpha} + \dot{\beta})\cos\alpha, \qquad \text{(A1)}$$

where μ measures the angular inertia of the arm relative to that of the attached mass. We see that β is a cyclic coordinate manifesting the freedom to shift the azimuthal angle about the pivot. The conserved momentum conjugate to β is

$$p_\beta = \frac{\partial L}{\partial \dot{\beta}} = 2\mu\dot{\beta} + (2\dot{\beta} + \dot{\alpha})(1 + \cos\alpha), \qquad \text{(A2)}$$

which is of course the total angular momentum of the mass and the arm. It is convenient to exploit this invariant to simplify the description of motion in the remaining degree of freedom. To this end, we construct the Routhian (Landau & Lifshitz 1969),

$$R = p_\beta\dot{\beta} - L. \qquad \text{(A3)}$$

After dropping a total time derivative, which will not contribute to the new action, we find

$$R = \frac{p_\beta^2 - \dot{\alpha}^2(2\mu + \sin^2\alpha)}{4(1+\cos\alpha+\mu)}. \tag{A4}$$

The equation of motion of α, describing the pivoting of the arm, is then obtained from the Routhian

$$\frac{d}{dt}\Big(\frac{\partial R}{\partial \dot{\alpha}}\Big) = \frac{\partial R}{\partial \alpha}, \tag{A5}$$

or directly from an energy integral

$$\begin{aligned} H =& R - \dot{\alpha}\frac{\partial R}{\partial \dot{\alpha}}, \\ =& \frac{p_\beta^2 + \dot{\alpha}^2(2\mu + \sin^2\alpha)}{4(1+\cos\alpha+\mu)}. \end{aligned} \tag{A6}$$

In the limit $\mu >> 1$, when the inertia of the arm is much greater than the attached mass, the librations reduce to that of the simple pendulum

$$\ddot{\alpha} = -\frac{p_\beta^2}{4\mu^2}\sin\alpha. \tag{A7}$$

We can see that the effect of the conserved momentum is to provide an effective potential for the swinging mass. The steady states of this system (analogous to the periodic orbits) correspond to the arm extended with $\alpha = 0$ (stable) or inwardly directed with $\alpha = \pi$ (unstable).

We can represent the possible motions of the system on a section through the phase space of the arm at fixed conserved momentum p_β. The ordinate in Fig. 21 is the energy integral

$$H = \frac{p_\beta^2}{4(1+\cos\alpha+\mu)} + \frac{(1+\cos\alpha+\mu)p_\alpha^2}{2\mu+\sin^2\alpha}. \tag{A8}$$

This energy integral is conserved so the trajectories oscillate along horizontal lines bounded by the confining envelope. These curves correspond to the trough ($\alpha = 0$) and the crest ($\alpha = \pi$) of the potential, where the kinetic energy of the attached mass is at a maximum or minimum. The greater the value of p_β, the greater the breadth of the envelope and consequently the broader the libration in p_α. The curvature of the envelope is dictated by the coefficient of p_α^2. There are motions of the attached mass in which it freely rotates about the joint pivot. There are motions too in which the mass librates about an outward pointing radius corresponding to the minimum of the effective centrifugal potential. These trapped motions lie in the basin of the section. In this region, we see that the section is internally bi-symmetric and dominated by a single harmonic. The envelope constricts at large p_α. There is an eventual cross-over of the lines of constant α (c.f., Fig. 11).

We can illustrate too the rôle that adiabatic invariants can play in the secular evolution of the system. Suppose the jointed arm, having been uniformly heated, is slowly returning to its natural length. We can anticipate that the system will conserve angular momentum and spin up as it shrinks. But, what happens to the libration of the attached mass as a function of the length $\ell(t)$ of the arm? We have implicitly removed a quadratic factor of length from the Lagrangian (A1) so that we can keep the equation of motion (A7) but with respect to a scaled time τ, such that

$$d\tau = \frac{dt}{\ell(t)^2}. \tag{A9}$$

As the arm shrinks, there is an effective increase in the centrifugal acceleration, but the angular range of the oscillation remains the same (as may easily be seen by integrating the equation of motion). In this process, it may not – for instance – pass from rotation to libration. Notice too that the action associated with the α oscillation is conserved exactly in this case. Suppose instead that the inner arm though contracting overall at the same rate as the outer has been heated differentially along its length. The re-distribution of mass may lead μ to be a slowly varying function of time. In this case, the action is only adiabatically invariant. Further, if μ is decreasing (for example, if the inner arm experiences greater heating close to the pivot), then the angular extent of the oscillation also decreases. The existence of the adiabatic invariant leads the mass to move closer to the minimum energy state in which the arm is straight and aligned radially outward.

7 APPENDIX B: CALCULATION OF THE REFINED CAPTURE PROBABILITY FORMULAE

This Appendix gives some more details of the computations leading to the capture probabilities presented in Section 3.4. Suppose the Hamiltonian is

$$\tilde{H} = \tilde{J}^2 - 2\lambda\tilde{J} - 2(2\tilde{J})^{1/2}(1-\epsilon\tilde{J})\cos\tilde{w}. \tag{B1}$$

The separatrix actions I are best evaluated using

$$I = \frac{1}{\pi}\oint \tilde{J}d\tilde{w} = \frac{1}{\pi}\oint \frac{\tilde{J}\dot{\tilde{w}}}{\dot{\tilde{J}}}d\tilde{J}, \tag{B2}$$

where the dots represent time derivatives and $\tilde{J}(w)$ is the equation of the separatrix. If the separatrix energy is $H_{\rm sep}$, then the numerator becomes

$$\begin{aligned} \tilde{J}\dot{\tilde{w}} =& \tfrac{3}{2}[1 - \tfrac{1}{9}\epsilon(8\lambda - 6\tilde{J})](\tilde{J} - \tilde{J}_u) \\ & \times [\tilde{J} + \tilde{J}_u - \tfrac{2}{3}\lambda - \tfrac{1}{27}\epsilon(24H_{\rm sep} + 16\lambda^2)], \end{aligned} \tag{B3}$$

where $\tilde{J}_u$ marks the position of the unstable fixed point. The denominator can be factorised as

$$\dot{\tilde{J}} = [(\tilde{J} - \tilde{J}_u)^2(\tilde{J}_2 - \tilde{J})(\tilde{J} - \tilde{J}_1)]^{1/2}. \tag{B4}$$

In other words, the unstable fixed point is always a double root, whereas the ends of the separatrix $\tilde{J}_1, \tilde{J}_2$ are single roots of the quartic. A lengthy calculation gives the areas under the separatrix branches as:

$$\begin{aligned} S_{\rm ret} =& \pi\lambda + 2\lambda\,{\rm asin}(x_\star^{-3/2}) + \frac{3(x_\star^3-1)^{1/2}}{x_\star} \\ & - \epsilon[\frac{3\pi x_\star}{2} + G_1(x_\star)], \\ S_{\rm prog} =& \pi\lambda - 2\lambda\,{\rm asin}(x_\star^{-3/2}) - \frac{3(x_\star^3-1)^{1/2}}{x_\star} \\ & - \epsilon[\frac{3\pi x_\star}{2} - G_1(x_\star)], \\ S_{\rm trap} =& 4\lambda\,{\rm asin}(x_\star^{-3/2}) + \frac{6(x_\star^3-1)^{1/2}}{x_\star}. \\ & - 2\epsilon G_1(x_\star), \end{aligned} \tag{B5}$$

where

$$G_1(x_\star) = 3\,\mathrm{asin}(x_\star^{-3/2}) + \frac{(2+x_\star^3)(x^3-1)^{1/2}}{x_\star^2}. \tag{B6}$$

Using (3.11) now gives the final result for the capture probability reported in the text as (3.38).

The addition of a second harmonic at the U-point leads to consideration of this Hamiltonian:

$$\tilde{H} = \tilde{J}^2 - 2\lambda\tilde{J} - 2(2\tilde{J})^{1/2}\cos\tilde{w} - \mu\tilde{J}\cos 2\tilde{w}, \tag{B7}$$

The areas under the separatrices are:

$$\begin{aligned}
S_{\mathrm{ret}} &= \pi\lambda + 2\lambda\,\mathrm{asin}(x_\star^{-3/2}) + \frac{3(x_\star^3-1)^{1/2}}{x_\star} \\
&\quad + \mu[\frac{\pi}{2}G_2(x_\star) + G_3(x_\star)], \\
S_{\mathrm{prog}} &= \pi\lambda - 2\lambda\,\mathrm{asin}(x_\star^{-3/2}) - \frac{3(x_\star^3-1)^{1/2}}{x_\star} \\
&\quad + \mu[\frac{\pi}{2}G_2(x_\star) - G_3(x_\star)], \\
S_{\mathrm{trap}} &= 4\lambda\,\mathrm{asin}(x_\star^{-3/2}) + \frac{6(x_\star^3-1)^{1/2}}{x_\star}. \\
&\quad + 2\mu G_3(x_\star),
\end{aligned} \tag{B8}$$

where

$$G_2(x_\star) = \frac{1}{36x_\star^3}\Big[x_\star^9 + 10x_\star^6 - 14x_\star^3 + 12\Big]. \tag{B9}$$

$$G_3(x_\star) = (x_\star^3-1)^{1/2}\Big[\frac{x_\star^3}{12} + \frac{1}{6x_\star^3}\Big] + G_2(x_\star)\,\mathrm{asin}(x_\star^{-3/2}). \tag{B10}$$

In this problem, $x_\star \geq 1$ correspond to those values for which there is a trapping region. The capture probability is given as (3.42).

This paper has been produced using the Royal Astronomical Society/Blackwell Science TEX macros.